Supplementary Information

Kinetic evolution of ZrO_2-modified silicate-based glass sealants during sintering and crystallization in planar solid oxide fuel cells

Shuai Yuan[a], Haozhen Li[a], Hao Shi[a], Yuxuan Fei[a], Hengyong Tu[a], Chao Ma[b, *], Lei Zhu[a, *], Zhen Huang[a,b]

[a] Key Laboratory for Power Machinery and Engineering of M.O.E., Shanghai Jiao Tong University, Shanghai 200240, China.

[b] College of Smart Energy, Shanghai Jiao Tong University, Shanghai 200240, China.

* Corresponding authors

E-mail addresses: chaoma99@sjtu.edu.cn (C. Ma), tonyzhulei@sjtu.edu.cn (L. Zhu).

E-mail addresses: chaoma99@sjtu.edu.cn（C. Ma）, tonyzhulei@sjtu.edu.cn（L. Zhu）.

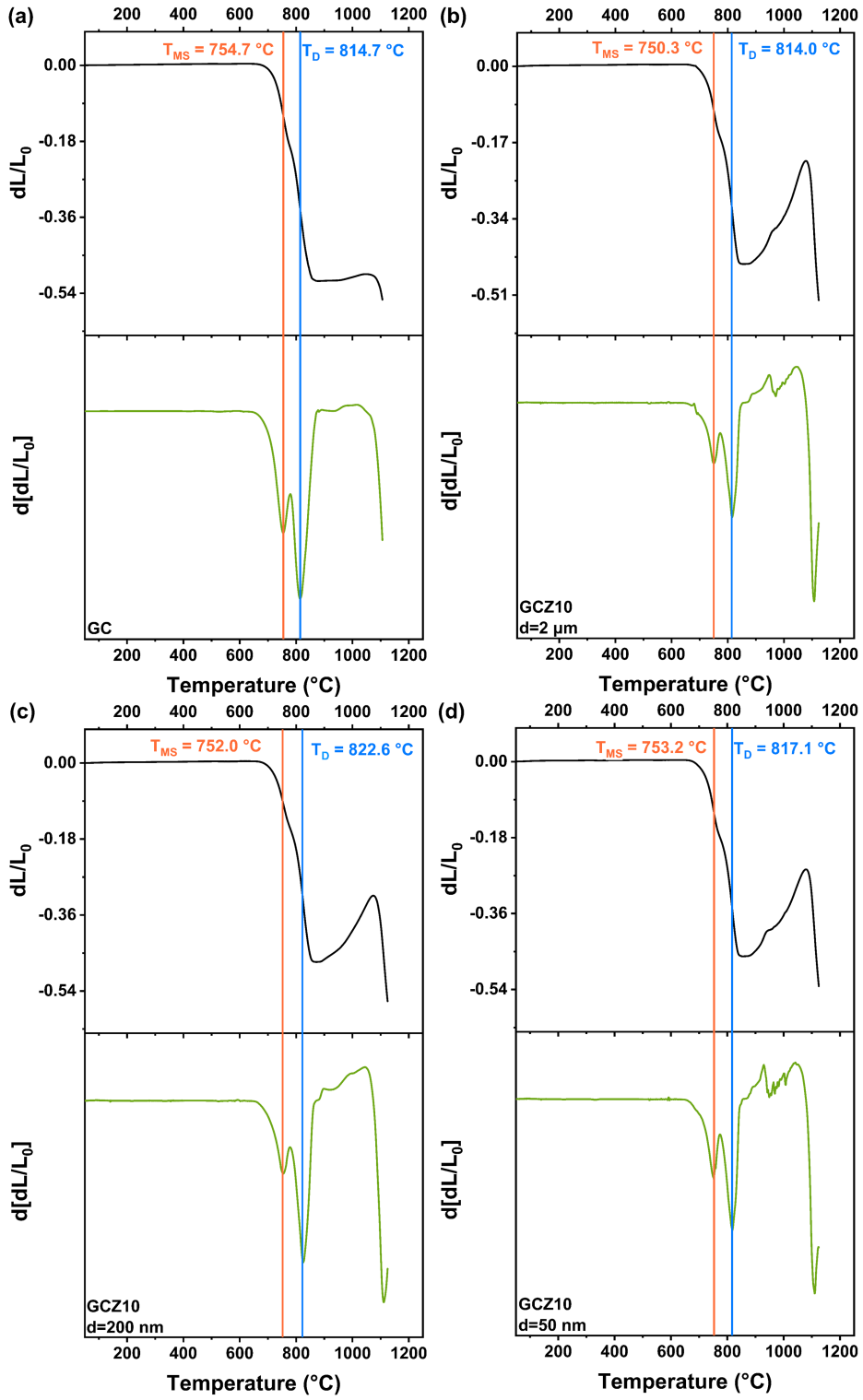

Fig. S1 Sintering curves and the first derivative curves of the sintering curves for (a) GC, (b) GCZ10, d=2 µm, (c) GCZ10, d=200 nm, (d) GCZ10, d=50 nm samples.

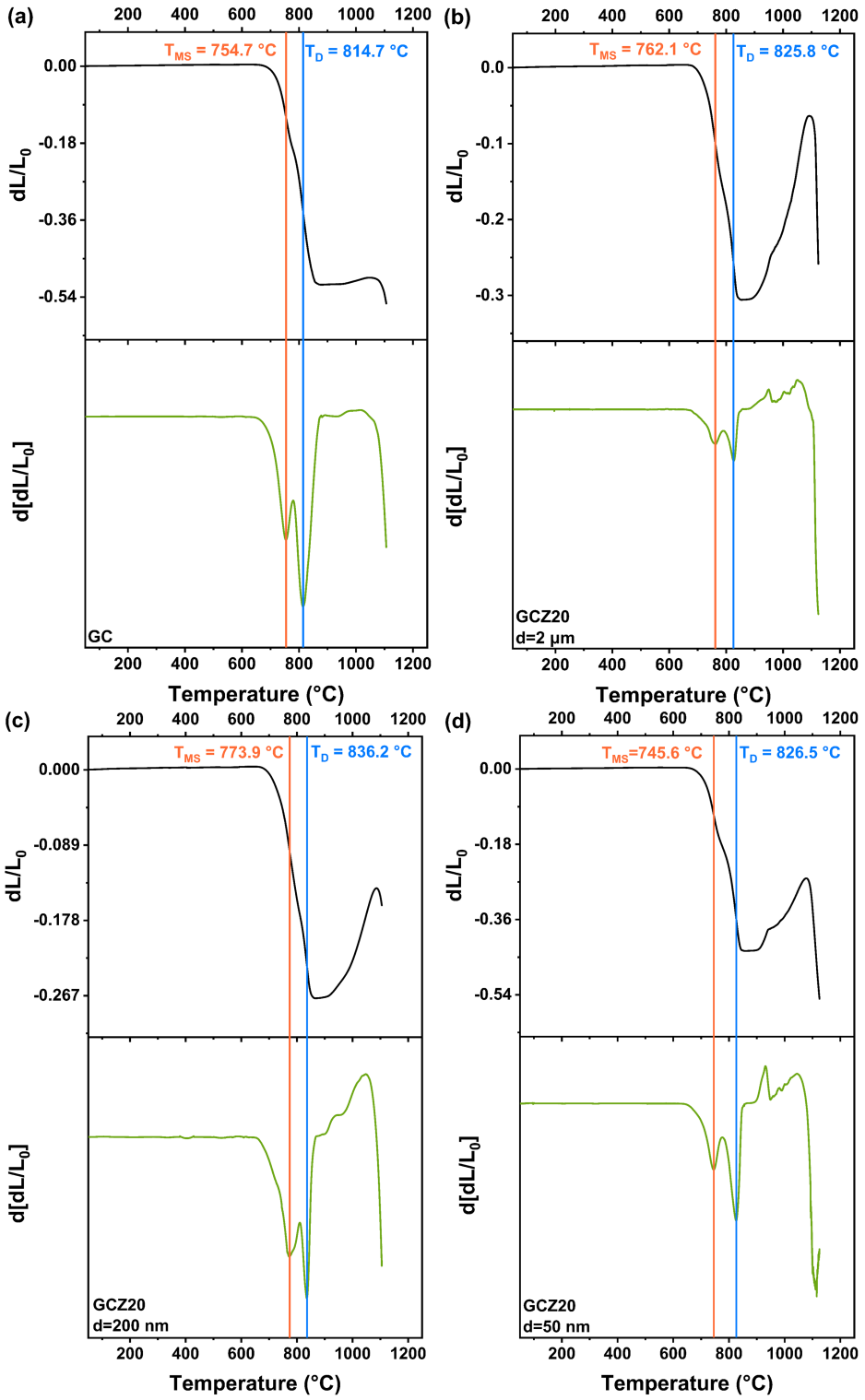

Fig. S2 Sintering curves and the first derivative curves of the sintering curves for (a) GC, (b) GCZ20, d=2 µm, (c) GCZ20, d=200 nm, (d) GCZ20, d=50 nm samples.

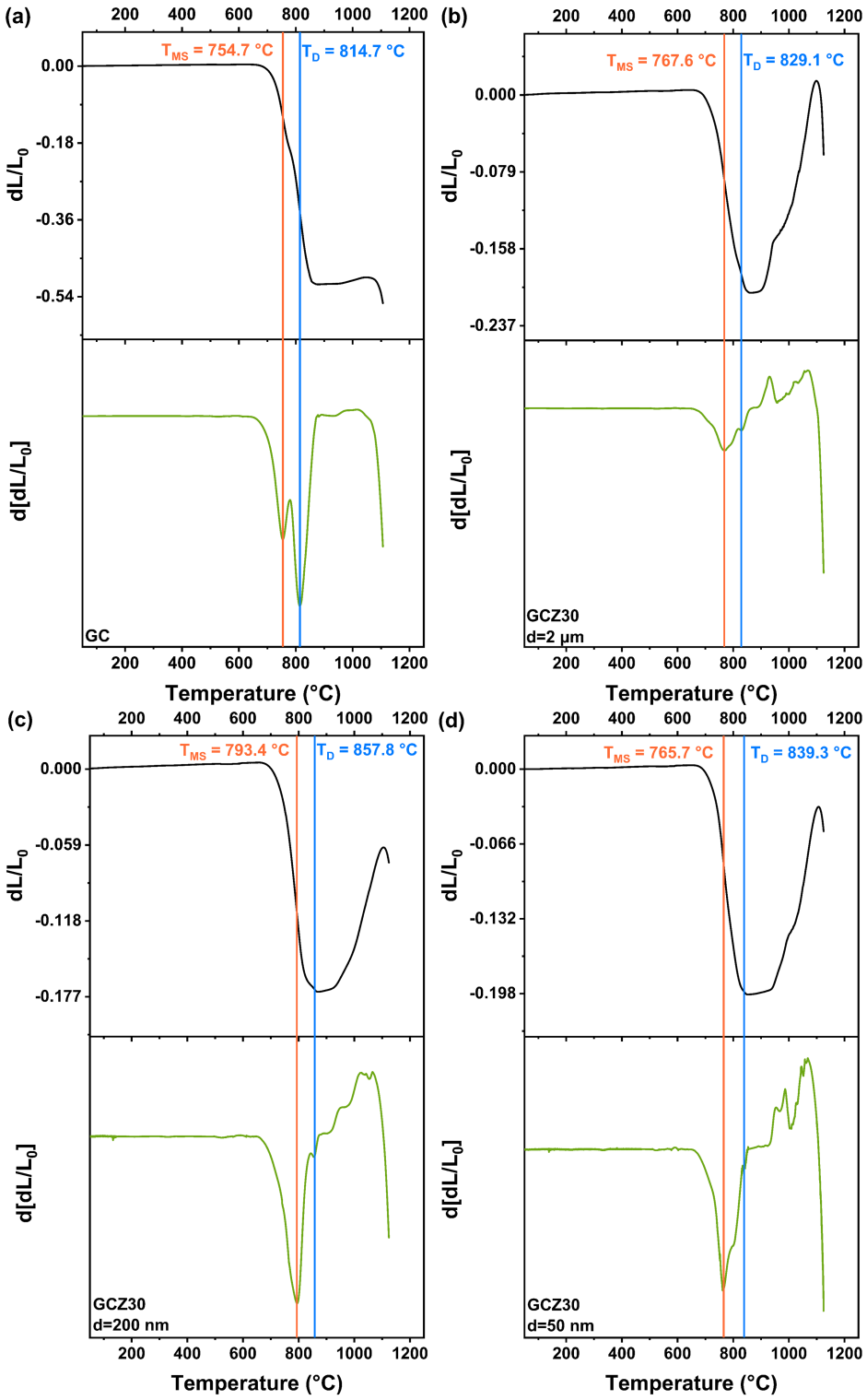

Fig. S3 Sintering curves and the first derivative curves of the sintering curves for (a) GC, (b) GCZ30, d=2 µm, (c) GCZ30, d=200 nm, (d) GCZ30, d=50 nm samples.

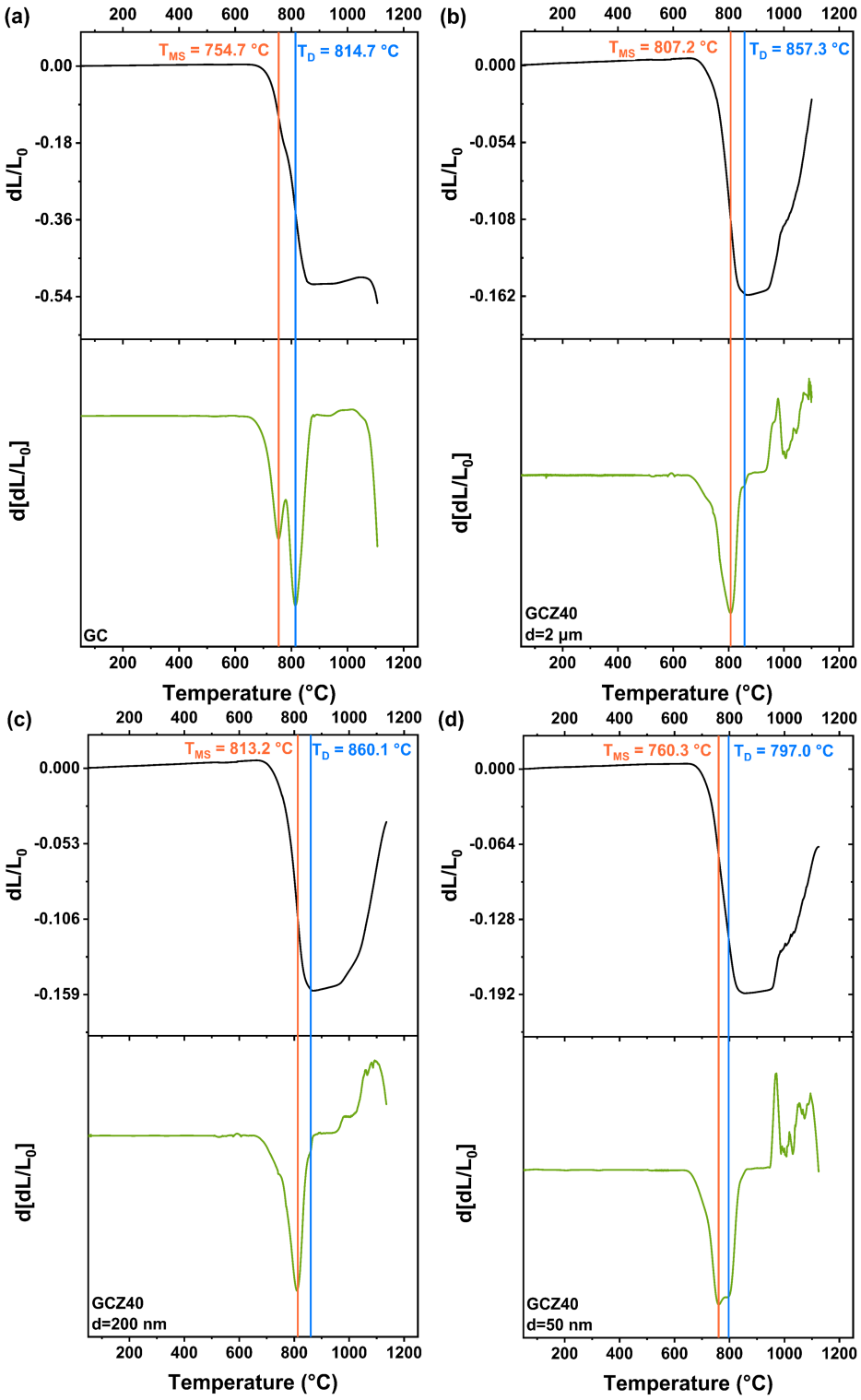

Fig. S4 Sintering curves and the first derivative curves of the sintering curves for (a) GC, (b) GCZ40, d=2 µm, (c) GCZ40, d=200 nm, (d) GCZ40, d=50 nm samples.

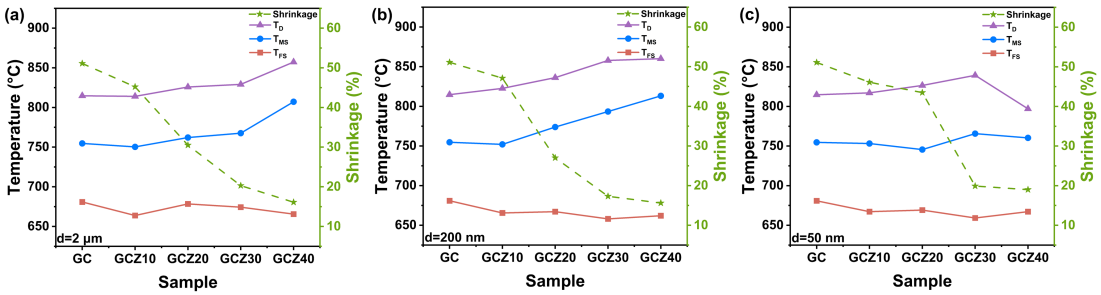

Fig. S5 Characteristic temperature and shrinkage rate for different mass fraction of (a) 2 μm ZrO_2, (b) 200 nm ZrO_2 and (c) 50 nm ZrO_2.

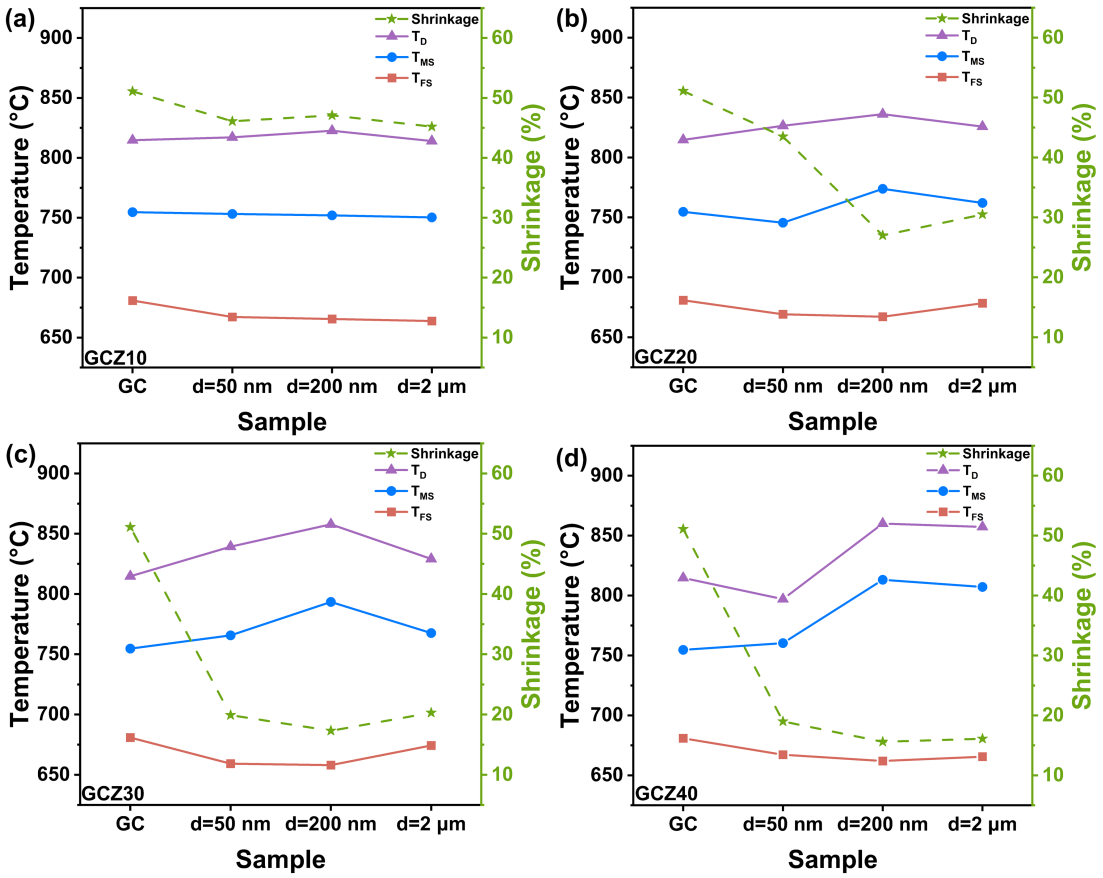

Fig. S6 Characteristic temperature and shrinkage rate for different particle sizes of (a) GCZ10, (b) GCZ20, (c) GCZ30 and (d) GCZ40 samples.

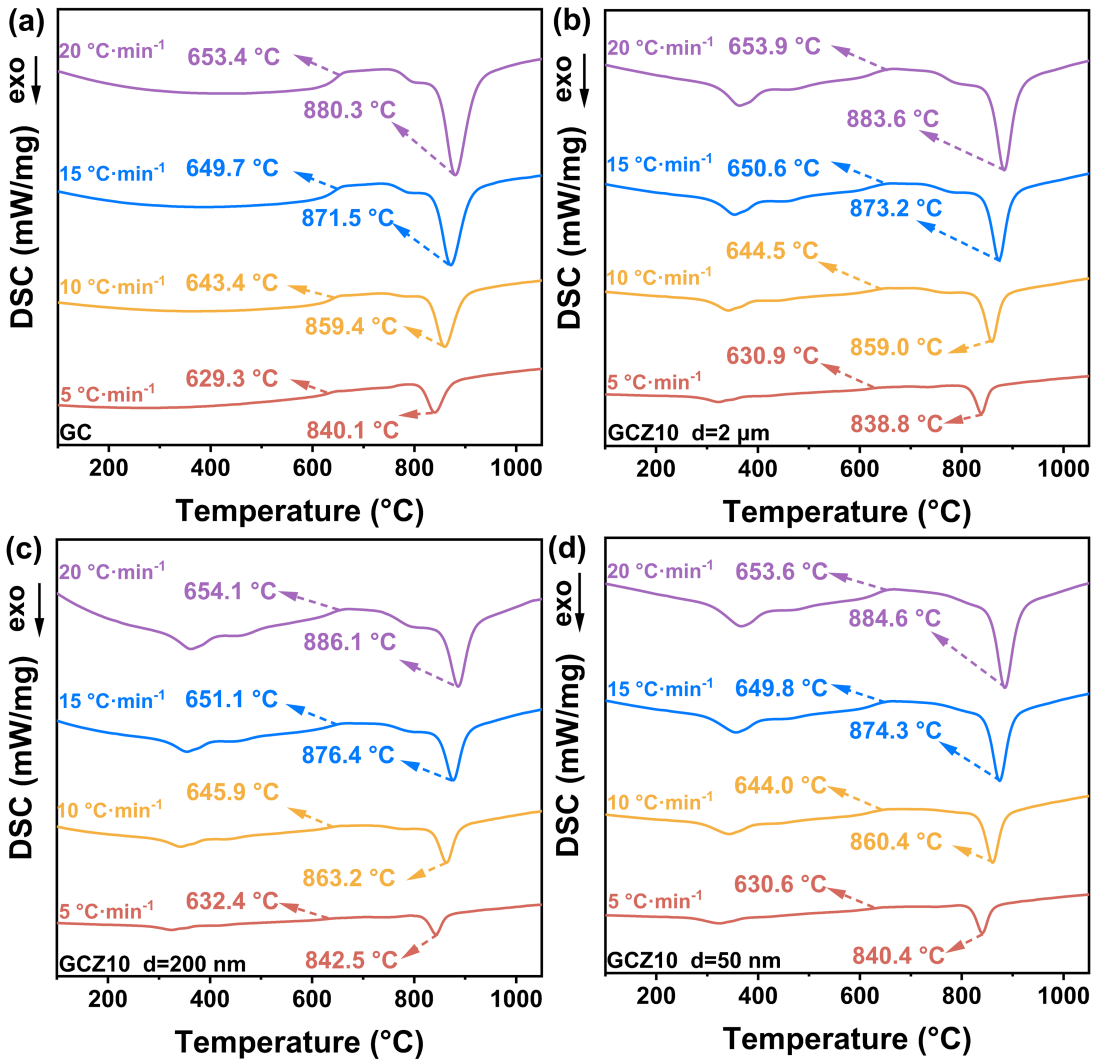

Fig. S7 DSC Curves obtained at different heating rates (5 °C·min^{-1}, 10 °C·min^{-1}, 15 °C·min^{-1}, 20 °C·min^{-1}) for (a) GC, (b) GCZ10, d=2 μm, (c) GCZ10, d=200 nm, (d) GCZ10, d=50 nm samples.

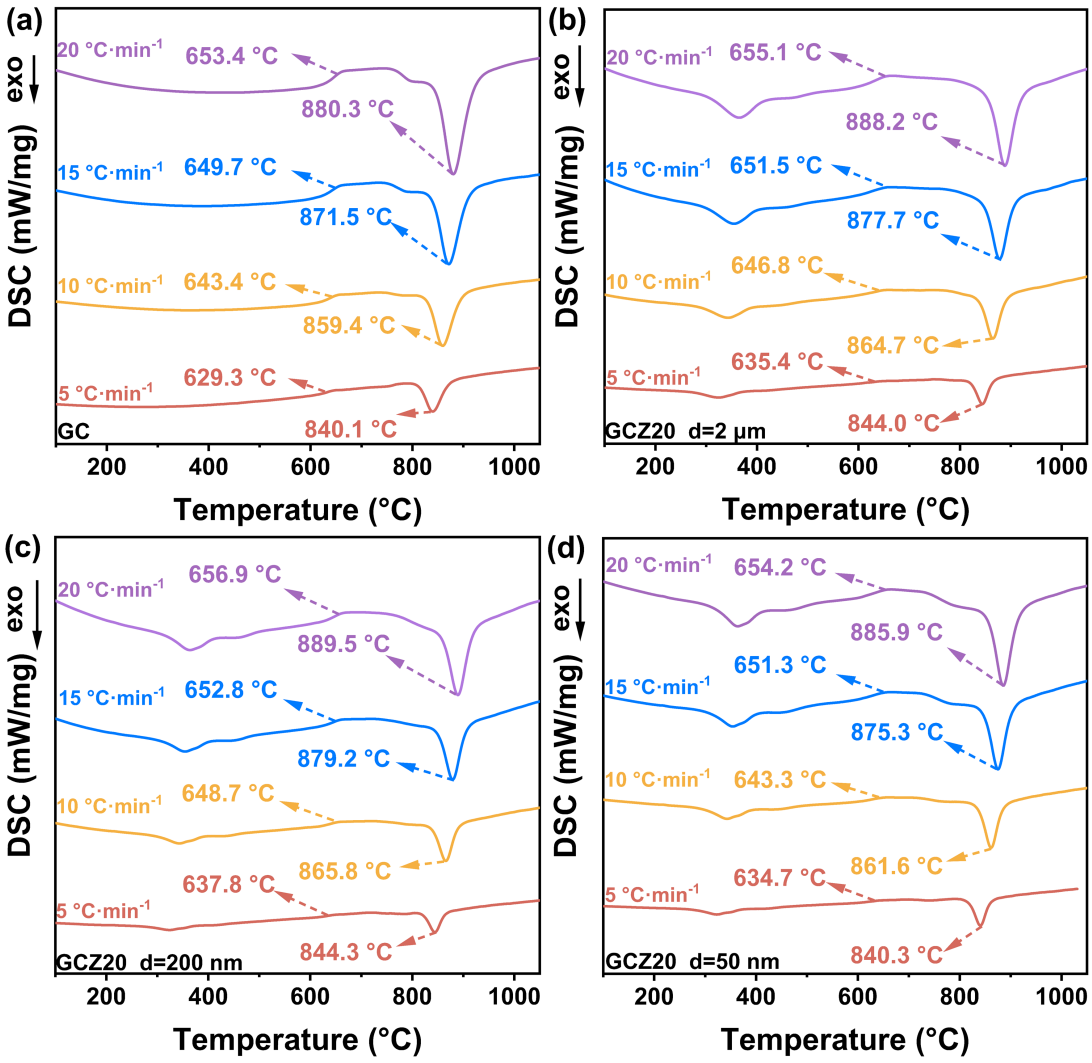

Fig. S8 DSC Curves obtained at different heating rates (5 °C·min^{-1}, 10 °C·min^{-1}, 15 °C·min^{-1}, 20 °C·min^{-1}) for (a) GC, (b) GCZ20, d=2 μm, (c) GCZ20, d=200 nm, (d) GCZ20, d=50 nm samples.

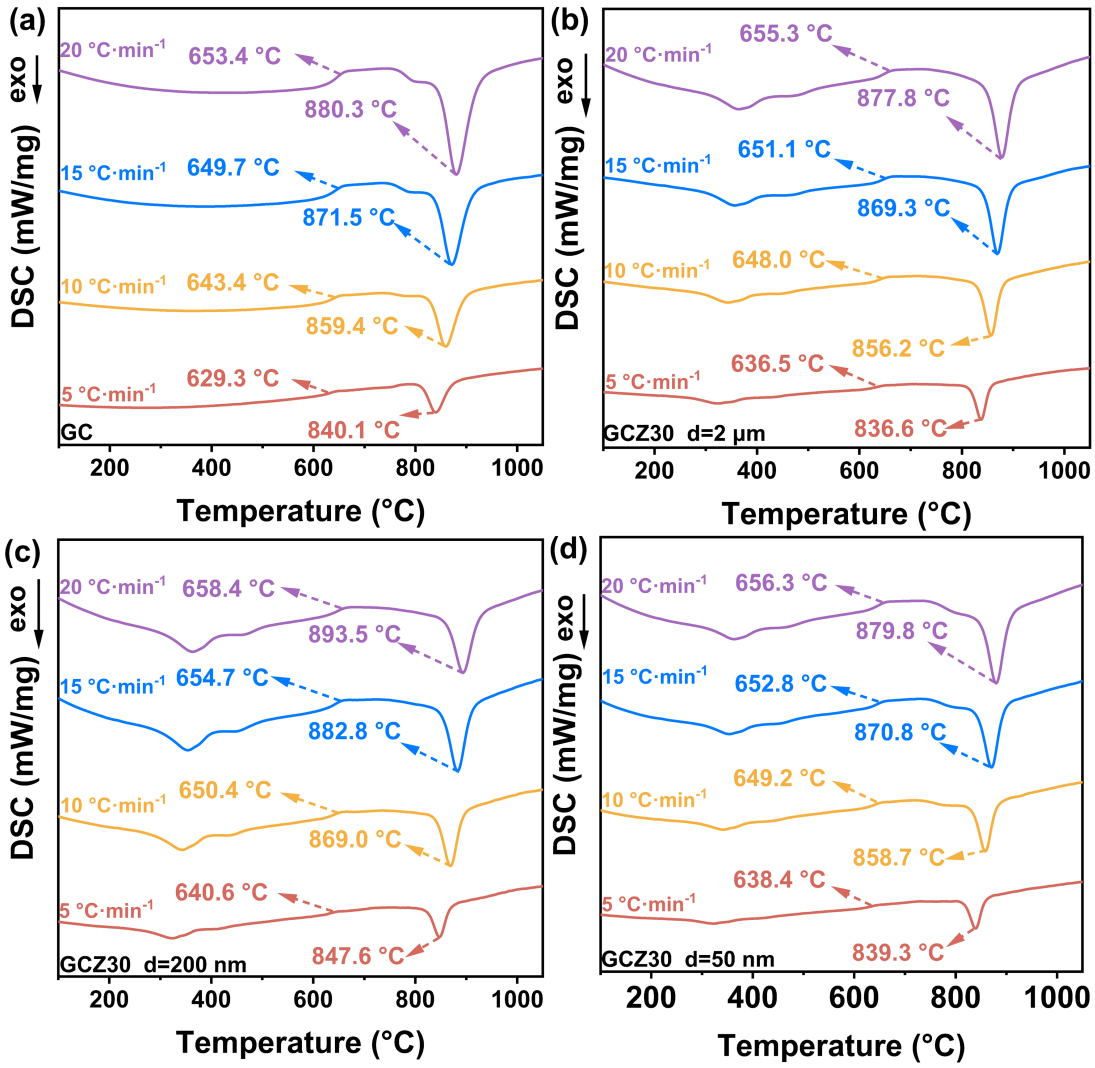

Fig. S9 DSC Curves obtained at different heating rates (5 °C·min^{-1}, 10 °C·min^{-1}, 15 °C·min^{-1}, 20 °C·min^{-1}) for (a) GC, (b) GCZ30, d=2 μm, (c) GCZ30, d=200 nm, (d) GCZ30, d=50 nm samples.

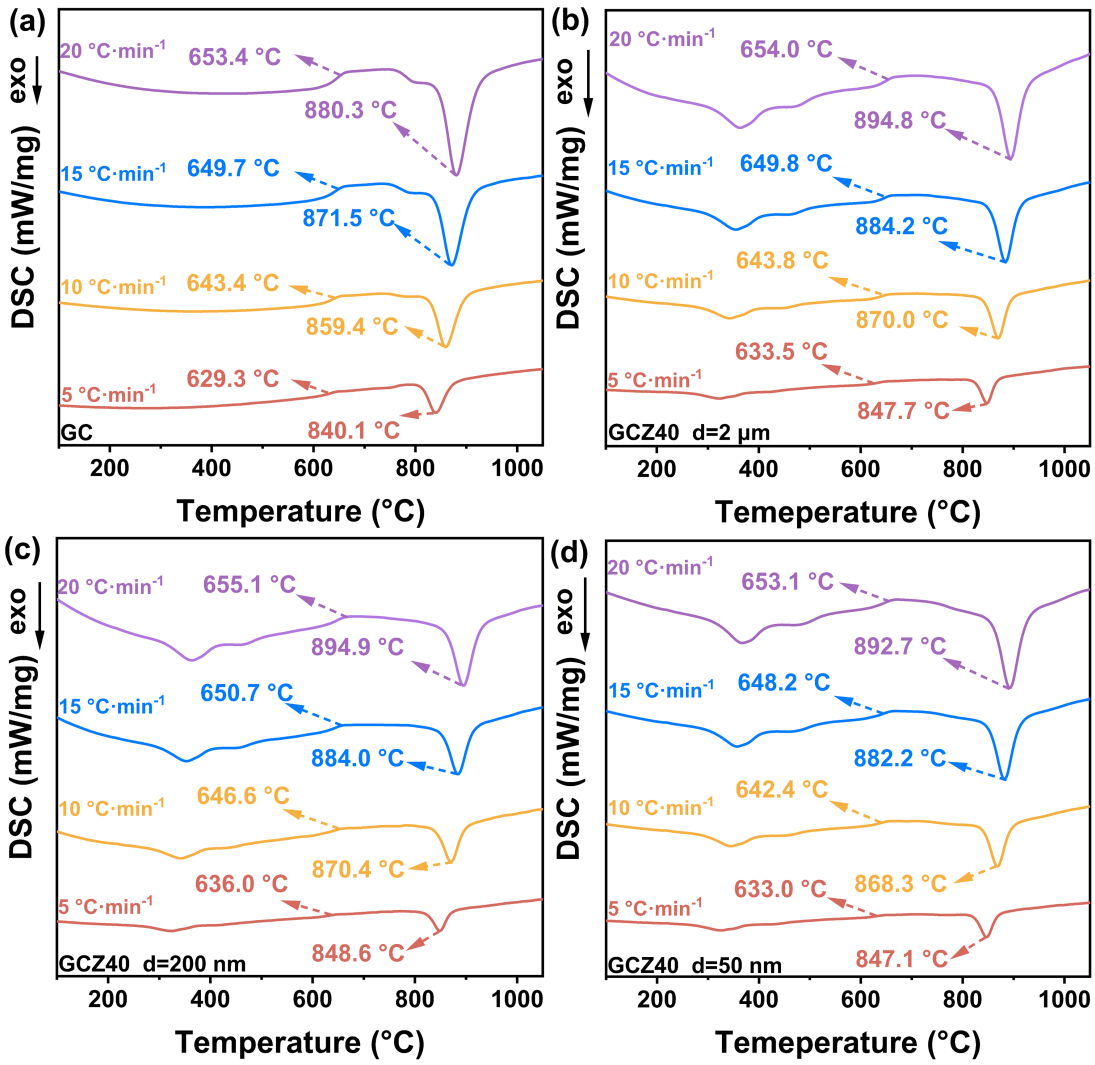

Fig. S10 DSC Curves obtained at different heating rates (5 °C·min^{-1}, 10 °C·min^{-1}, 15 °C·min^{-1}, 20 °C·min^{-1}) for (a) GC, (b) GCZ40, d=2 μm, (c) GCZ40, d=200 nm, (d) GCZ40, d=50 nm samples.

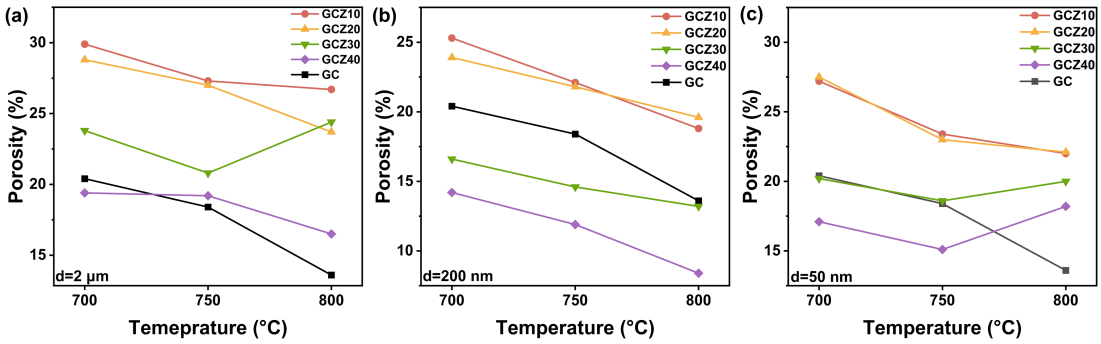

Fig. S11 Porosity for different mass fraction of (a) 2 μm ZrO_2, (b) 200 nm ZrO_2 and (c) 50 nm ZrO_2 at 700 ºC, 750 ºC, and 800 ºC.

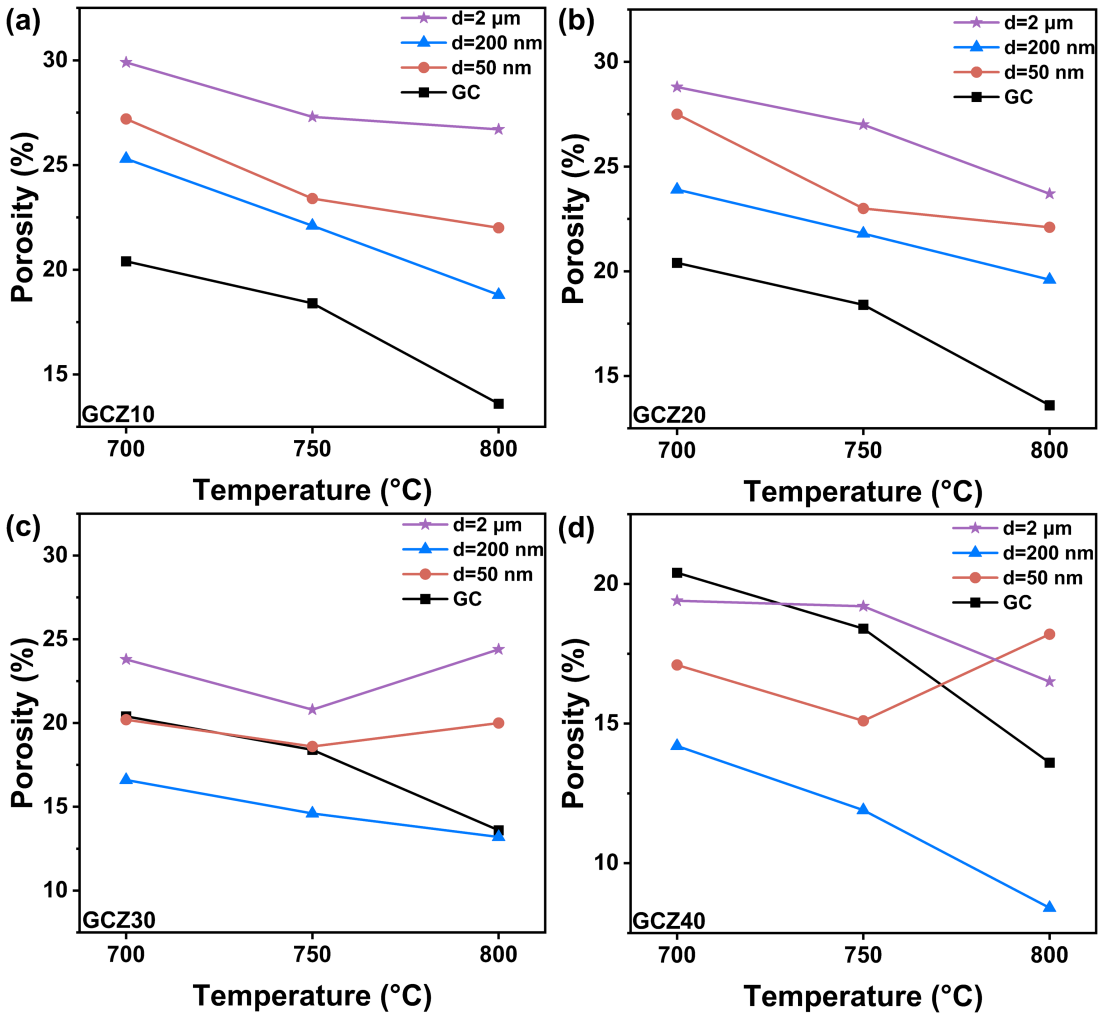

Fig. S12 Porosity for different particle sizes of (a) GCZ10, (b) GCZ20, (c) GCZ30 and (d) GCZ40 samples at 700 ºC, 750 ºC, and 800 ºC.

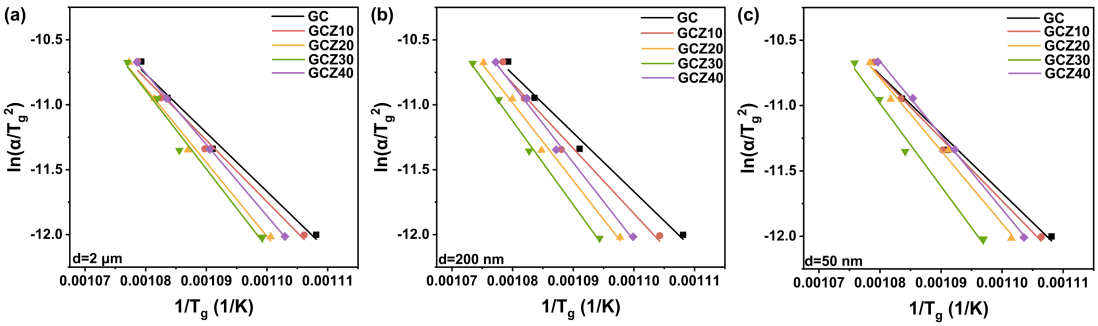

Fig. S13 Plots of $\ln(\alpha/T_g^2)$ versus $1/T_g$ for different mass fraction of (a) 2 μm ZrO_2, (b) 200 nm ZrO_2 and (c) 50 nm ZrO_2.

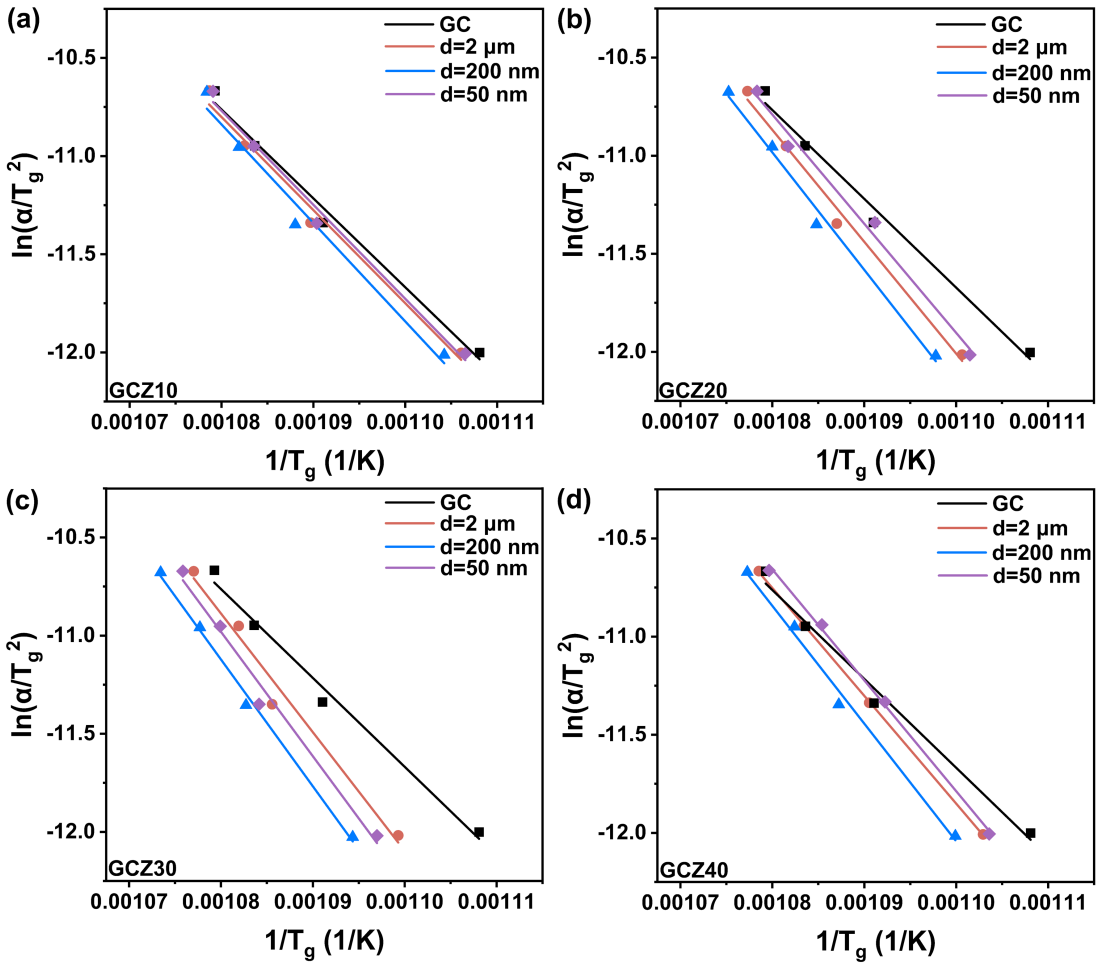

Fig. S14 Plots of $\ln(\alpha/T_g^2)$ versus $1/T_g$ for different particle sizes of (a) GCZ10, (b) GCZ20, (c) GCZ30 and (d) GCZ40 samples.

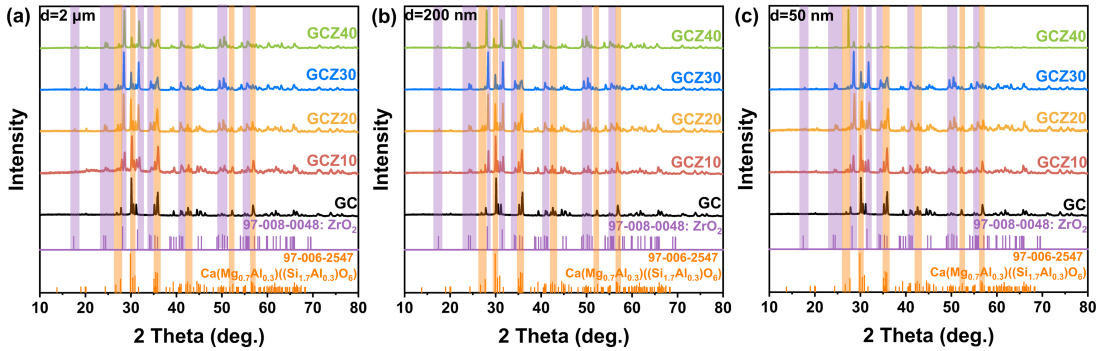

Fig. S15 XRD patterns for different mass fraction of (a) 2 μm ZrO_2, (b) 200 nm ZrO_2 and (c) 50 nm ZrO_2 after heat-treatment for 20 hours.

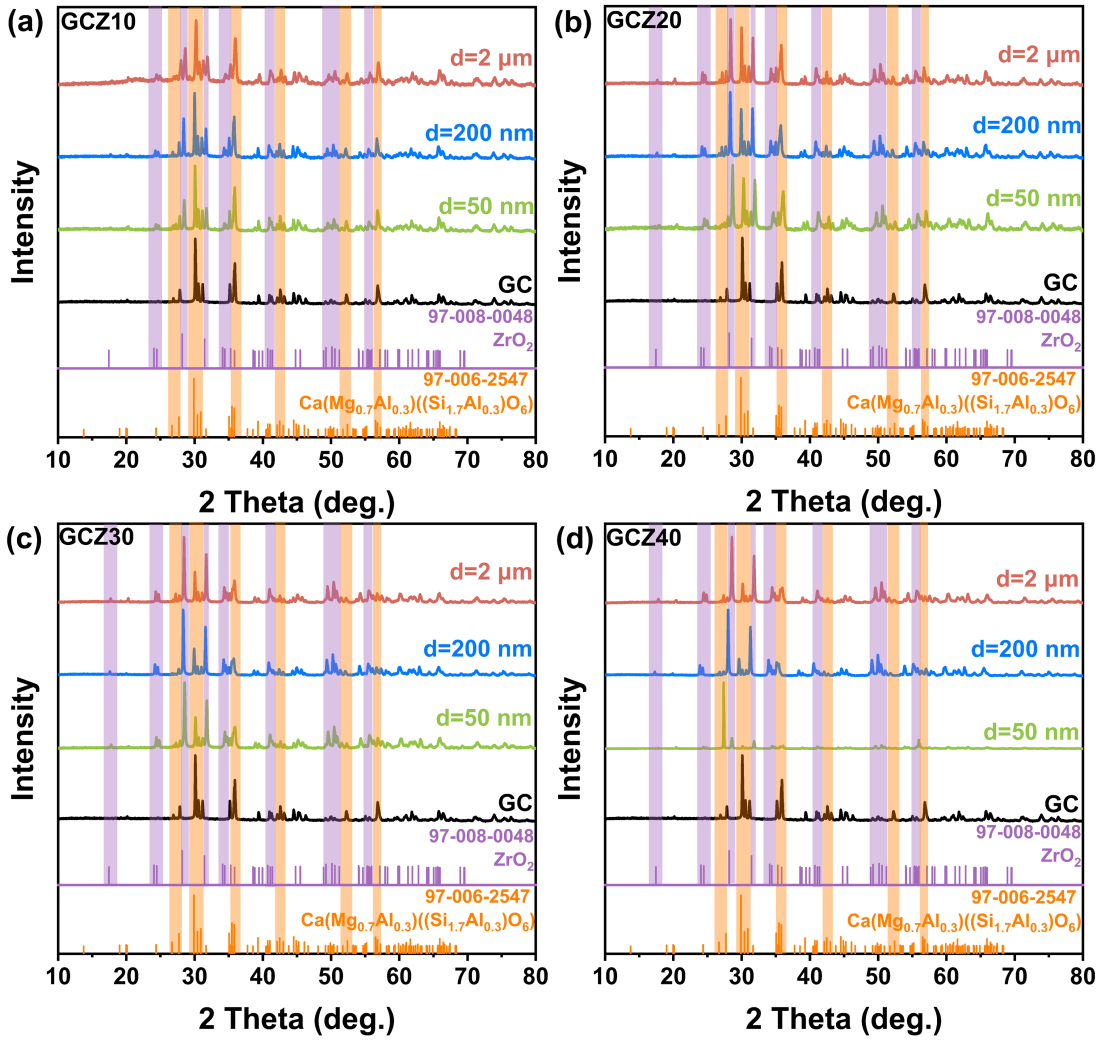

Fig. S16 XRD patterns for different particle sizes of (a) GCZ10, (b) GCZ20, (c) GCZ30 and (d) GCZ40 samples after heat-treatment for 20 hours.

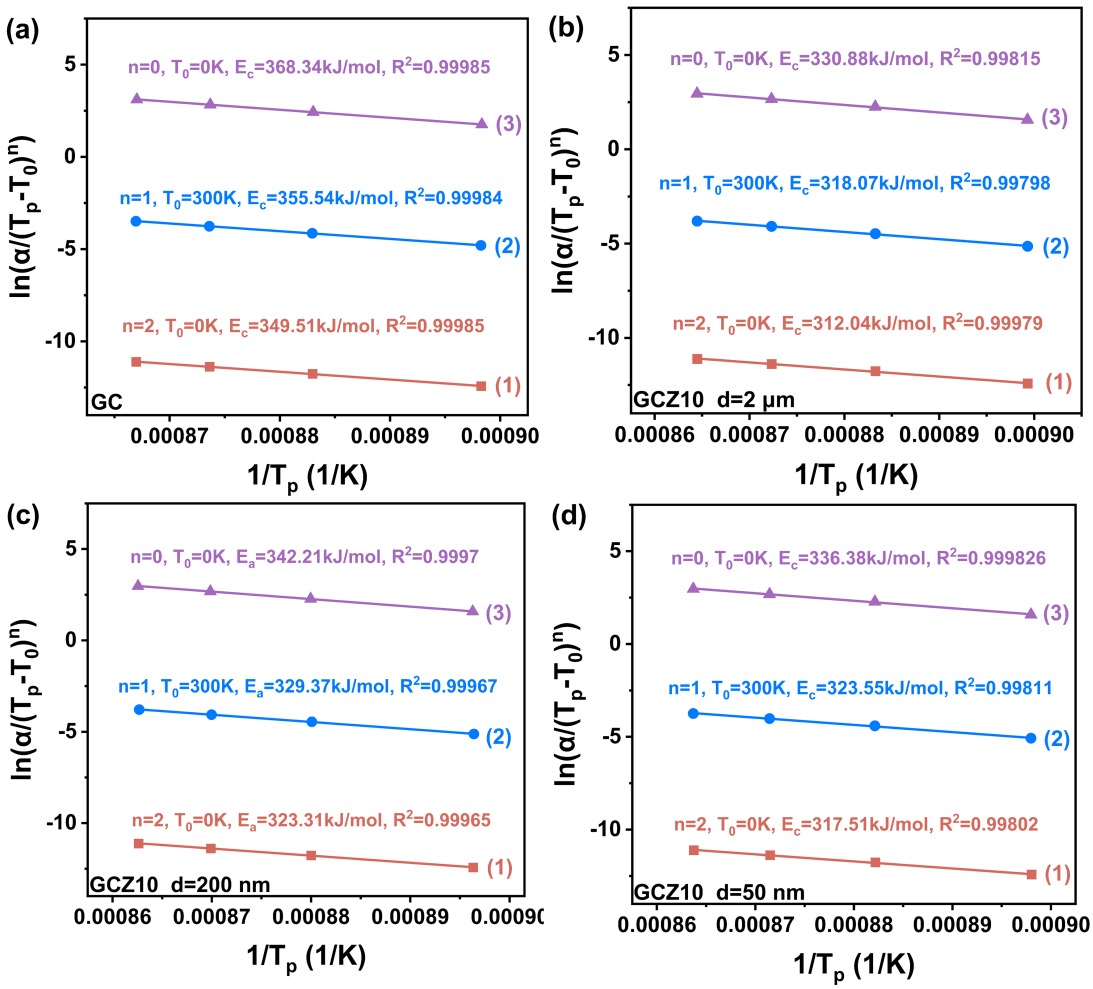

Fig. S17 Plots of $\ln\left(\alpha/(T_p - T_0)^n\right)$ versus $1/T_p$ calculated based on (1) Kissinger model, (2) Augis-Bennett model and (3) Ozawa model for (a) GC, (b) GCZ10, d=2 μm, (c) GCZ10, d=200 nm, (d) GCZ10, d=50 nm samples.

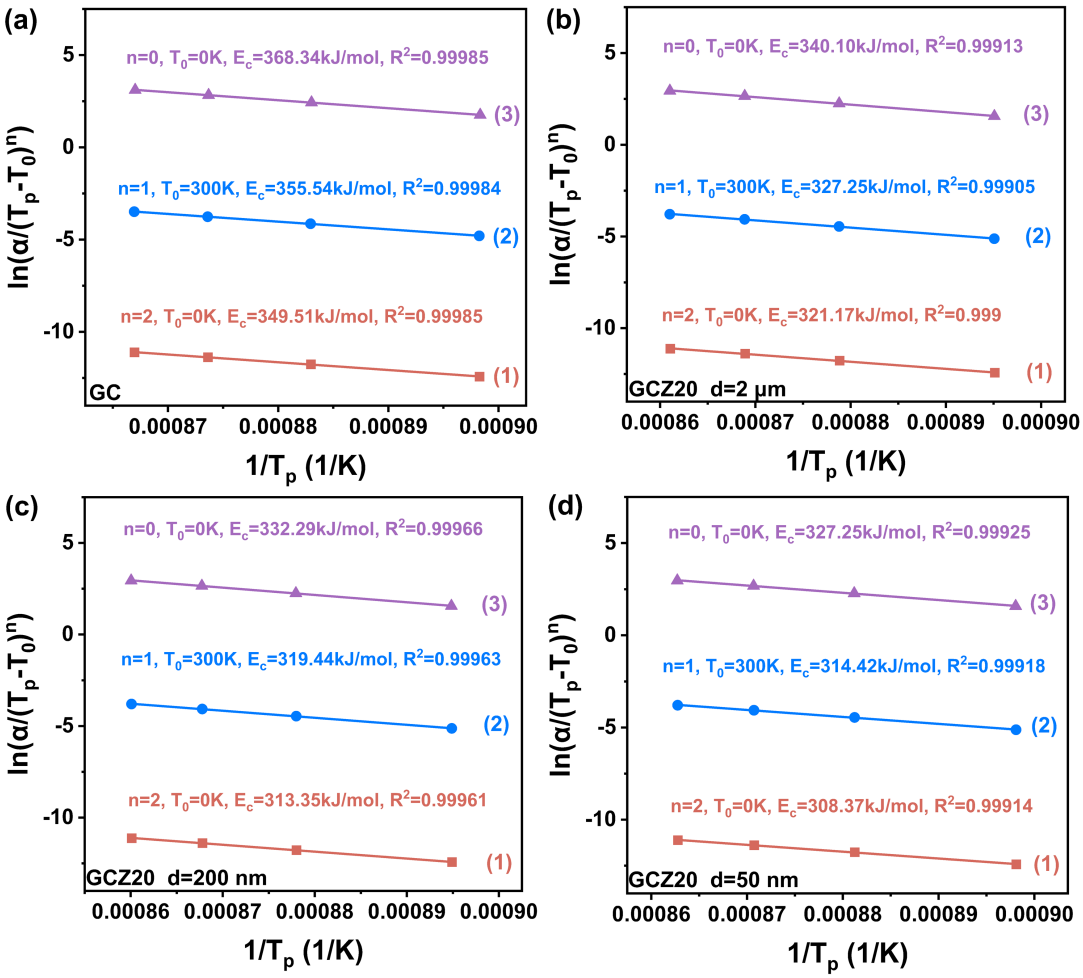

Fig. S18 Plots of $\ln(\alpha/(T_p - T_0)^n)$ versus $1/T_p$ calculated based on (1) Kissinger model, (2) Augis-Bennett model and (3) Ozawa model for (a) GC, (b) GCZ20, d=2 μm, (c) GCZ20, d=200 nm, (d) GCZ20, d=50 nm samples.

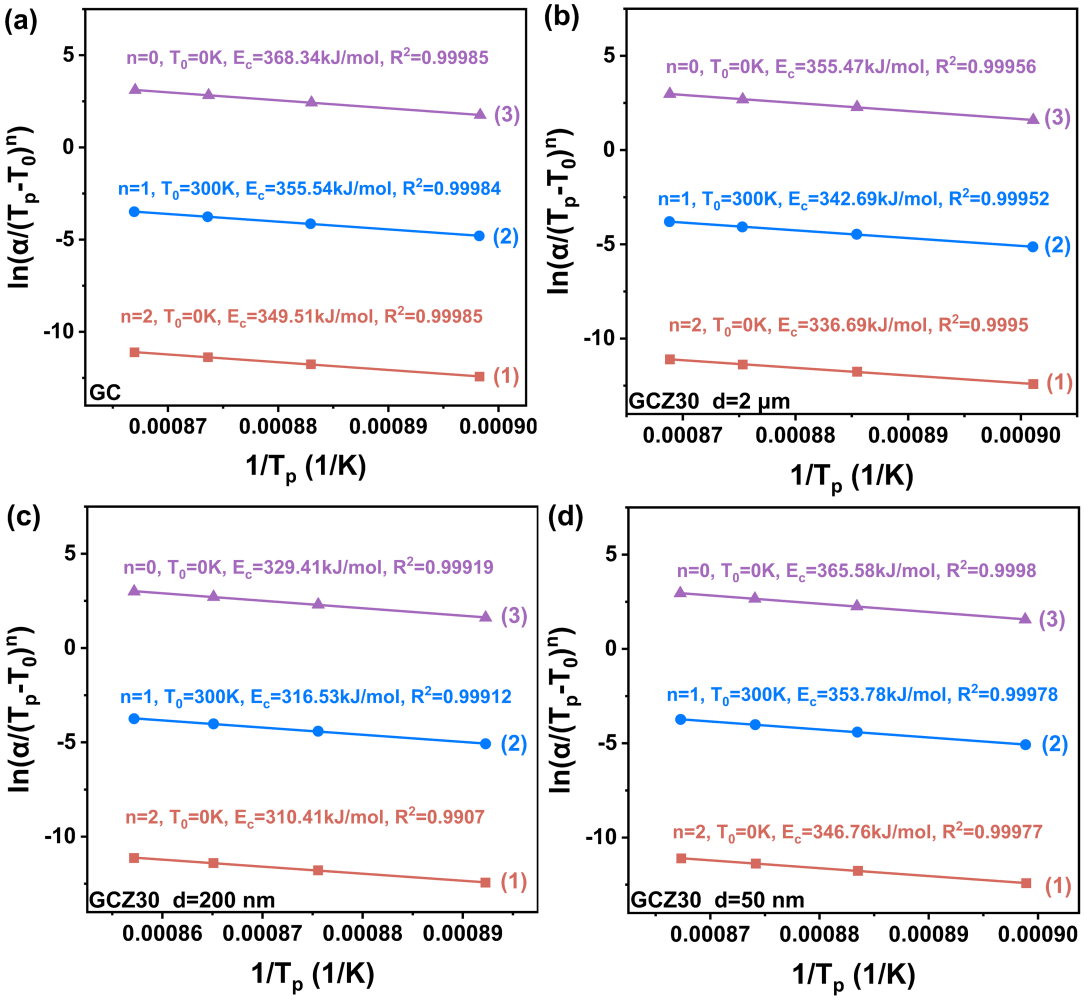

Fig. S19 Plots of $\ln\left(\alpha/(T_p - T_0)^n\right)$ versus $1/T_p$ calculated based on (1) Kissinger model, (2) Augis-Bennett model and (3) Ozawa model for (a) GC, (b) GCZ30, d=2 μm, (c) GCZ30, d=200 nm, (d) GCZ30, d=50 nm samples.

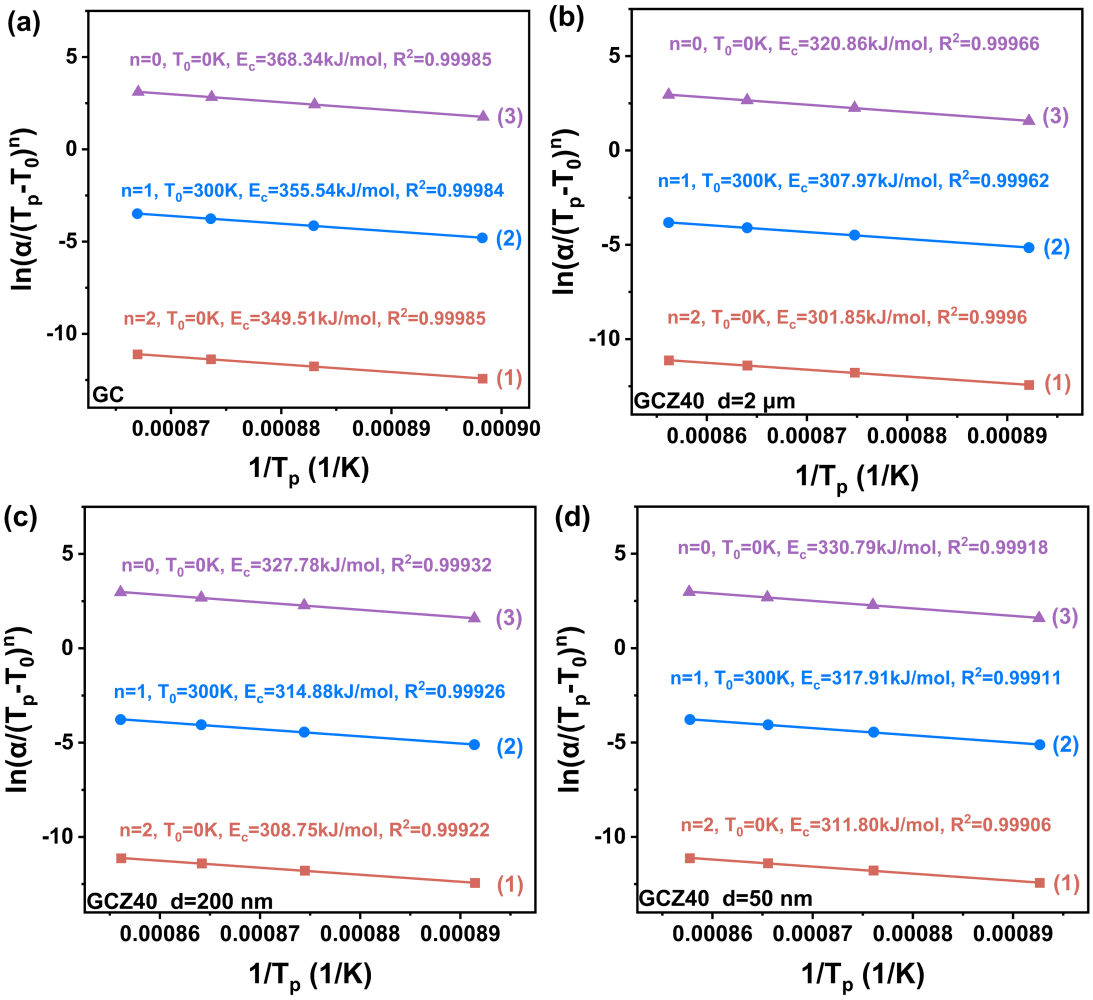

Fig. S20 Plots of $\ln(\alpha/(T_p - T_0)^n)$ versus $1/T_p$ calculated based on (1) Kissinger model, (2) Augis-Bennett model and (3) Ozawa model for (a) GC, (b) GCZ40, d=2 μm, (c) GCZ40, d=200 nm, (d) GCZ40, d=50 nm samples.

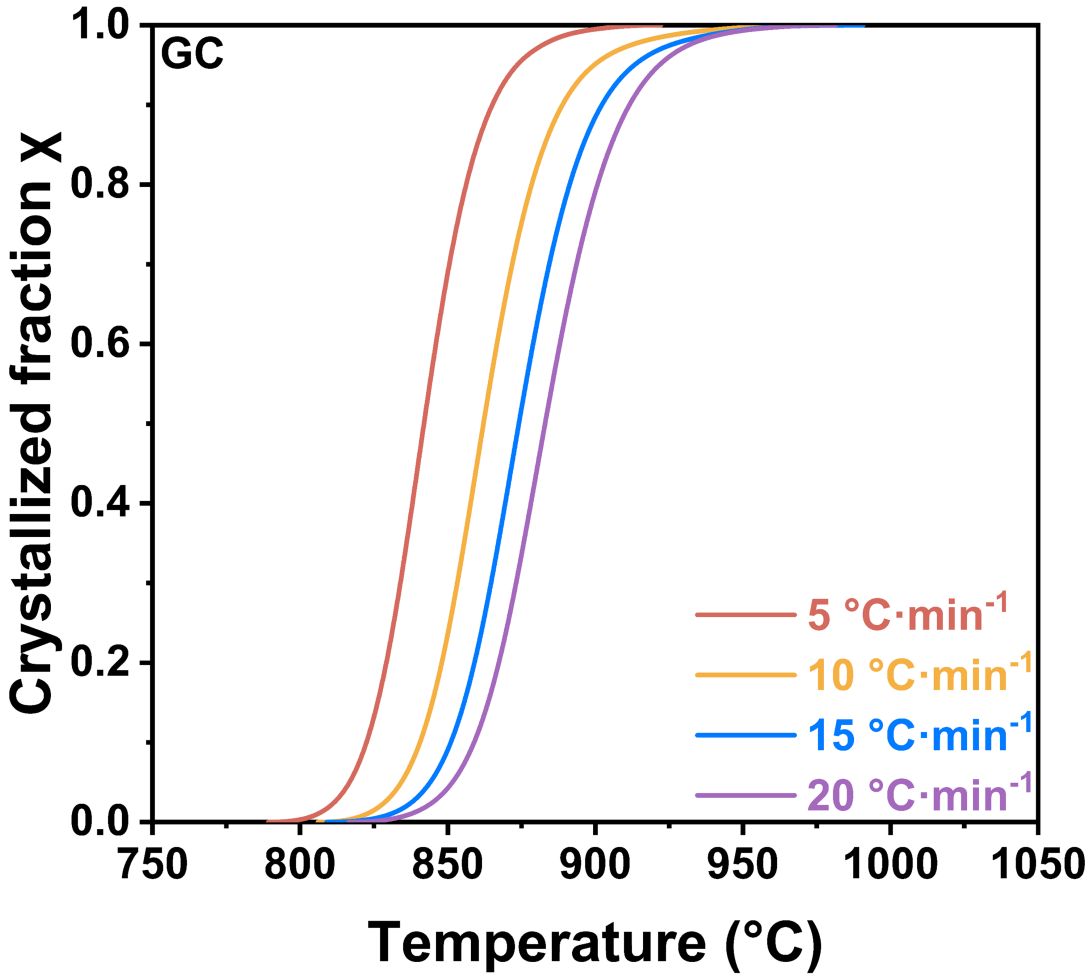

Fig. S21 Crystallized fraction χ as a function of temperature at different heating rates (5 ℃·min^{-1}, 10 ℃·min^{-1}, 15 ℃·min^{-1}, 20 ℃·min^{-1}) for GC.

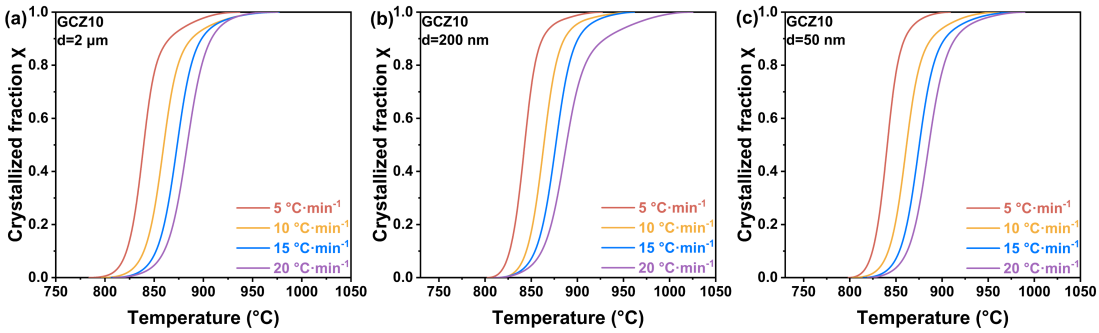

Fig. S22 Crystallized fraction χ as a function of temperature at different heating rates (5 °C·min^{-1}, 10 °C·min^{-1}, 15 °C·min^{-1}, 20 °C·min^{-1}) for (a) GCZ10, d=2 μm, (b) GCZ10, d=200 nm and (c) GCZ10, d=50 nm samples.

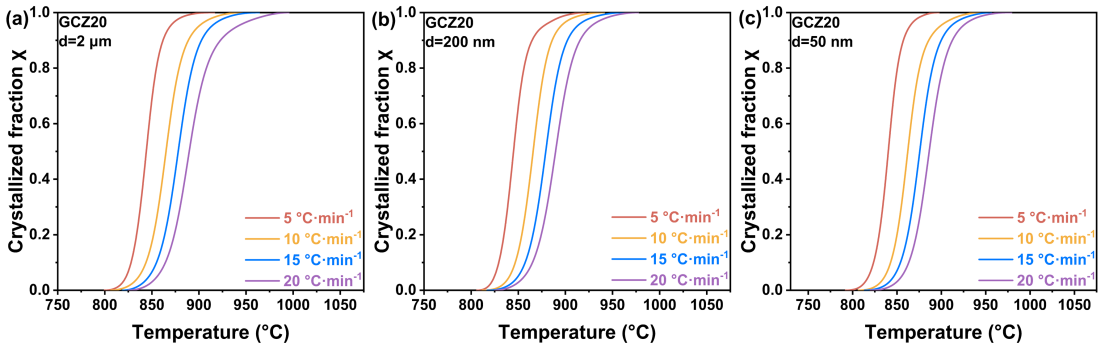

Fig. S23 Crystallized fraction χ as a function of temperature at different heating rates (5 °C·min^{-1}, 10 °C·min^{-1}, 15 °C·min^{-1}, 20 °C·min^{-1}) for (a) GCZ20, d=2 μm, (b) GCZ20, d=200 nm and (c) GCZ20, d=50 nm samples.

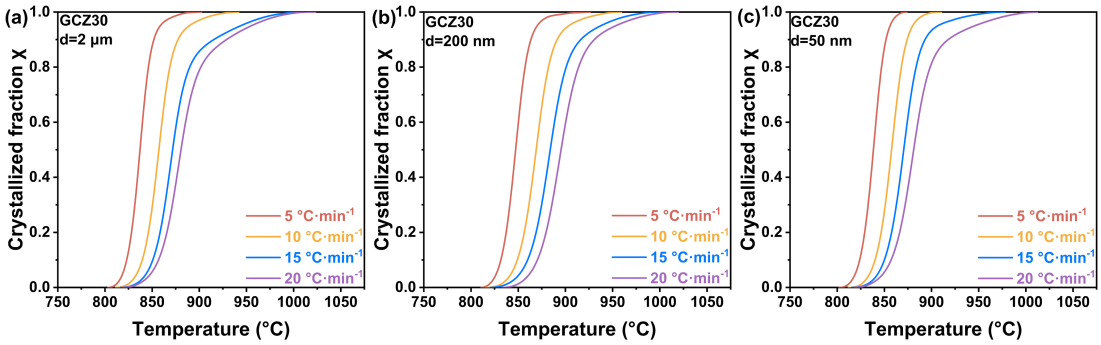

Fig. S24 Crystallized fraction χ as a function of temperature at different heating rates (5 °C·min^{-1}, 10 °C·min^{-1}, 15 °C·min^{-1}, 20 °C·min^{-1}) for (a) GCZ30, d=2 µm, (b) GCZ30, d=200 nm and (c) GCZ30, d=50 nm samples.

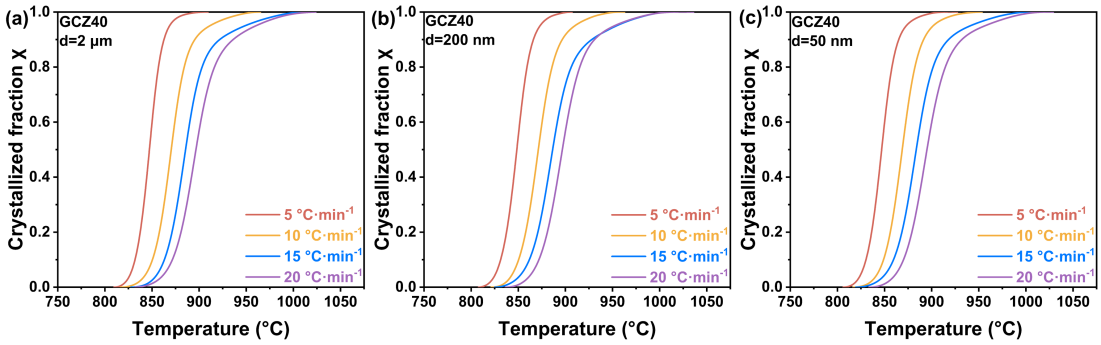

Fig. S25 Crystallized fraction χ as a function of temperature at different heating rates (5 °C·min^{-1}, 10 °C·min^{-1}, 15 °C·min^{-1}, 20 °C·min^{-1}) for (a) GCZ40, d=2 µm, (b) GCZ40, d=200 nm and (c) GCZ40, d=50 nm samples.

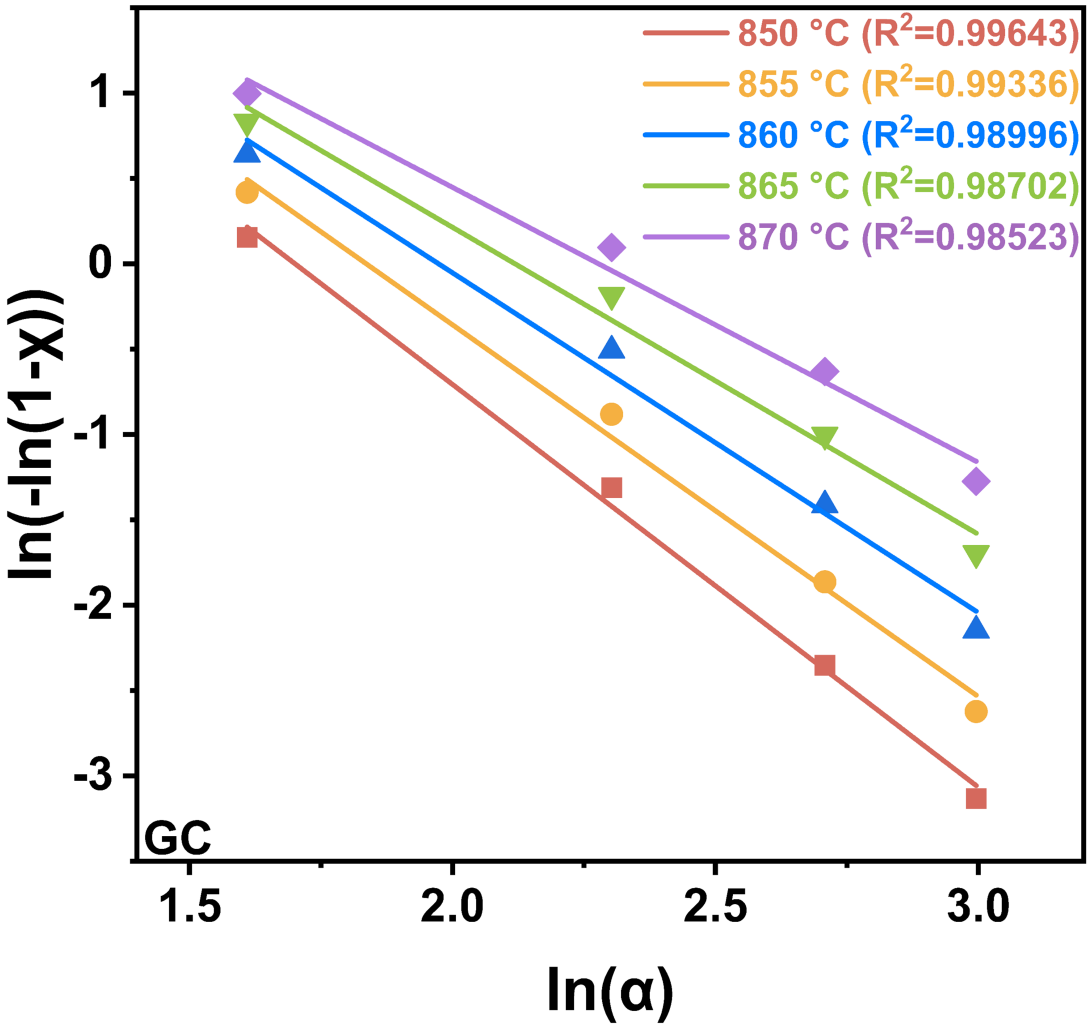

Fig. S26 Plot of $\ln(-\ln(1-x))$ versus $\ln\alpha$ at fixed temperatures determined by Ozawa equation for GC.

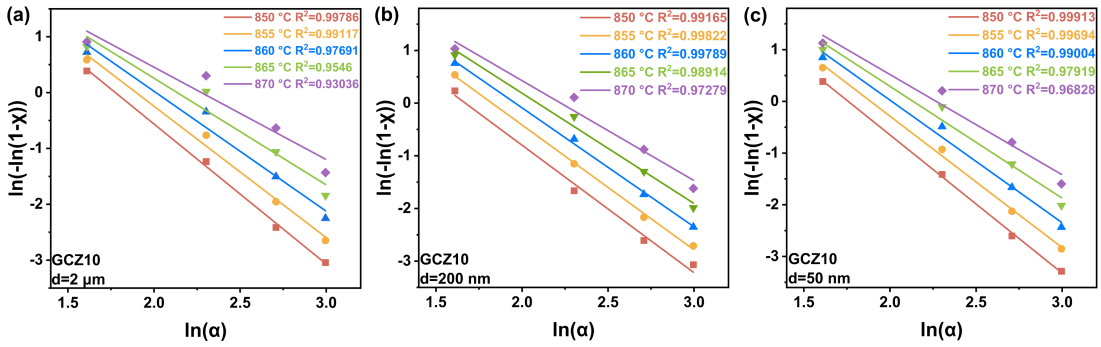

Fig. S27 Plots of $\ln(-\ln(1-x))$ versus $\ln\alpha$ at fixed temperatures determined by Ozawa equation for (a) GCZ10, d=2 μm, (b) GCZ10, d=200 nm and (c) GCZ10, d=50 nm samples.

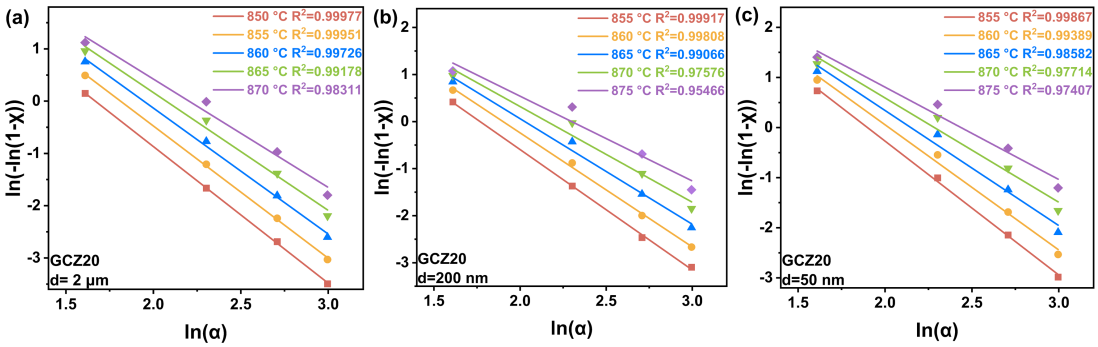

Fig. S28 Plots of $\ln(-\ln(1-x))$ versus $\ln\alpha$ at fixed temperatures determined by Ozawa equation for (a) GCZ20, d=2 μm, (b) GCZ20, d=200 nm and (c) GCZ20, d=50 nm samples.

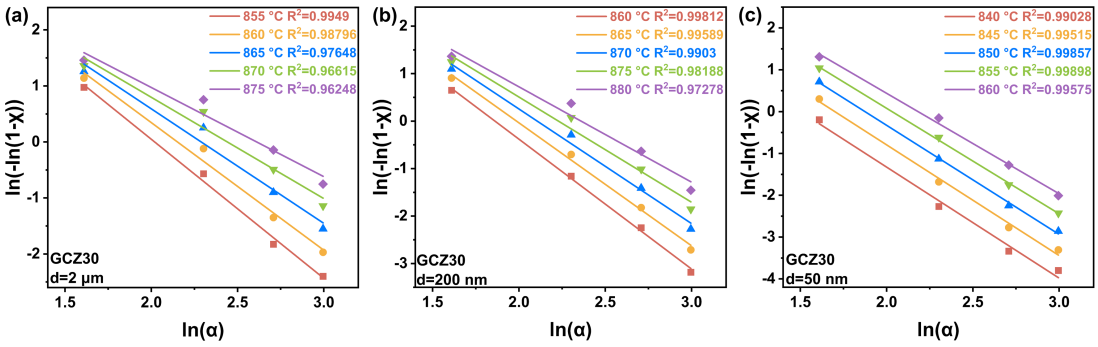

Fig. S29 Plots of $\ln(-\ln(1-x))$ versus $\ln\alpha$ at fixed temperatures determined by Ozawa equation for (a) GCZ30, d=2 μm, (b) GCZ30, d=200 nm and (c) GCZ30, d=50 nm samples.

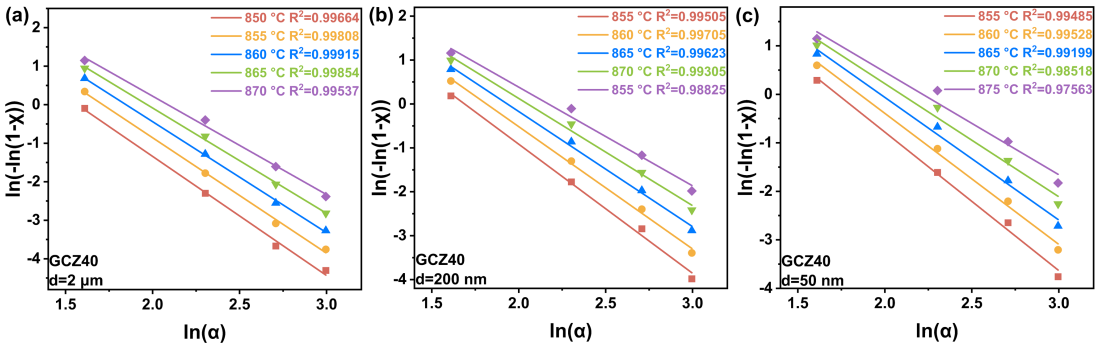

Fig. S30 Plots of $\ln(-\ln(1-x))$ versus $\ln\alpha$ at fixed temperatures determined by Ozawa equation for (a) GCZ40, d=2 μm, (b) GCZ40, d=200 nm and (c) GCZ40, d=50 nm samples.

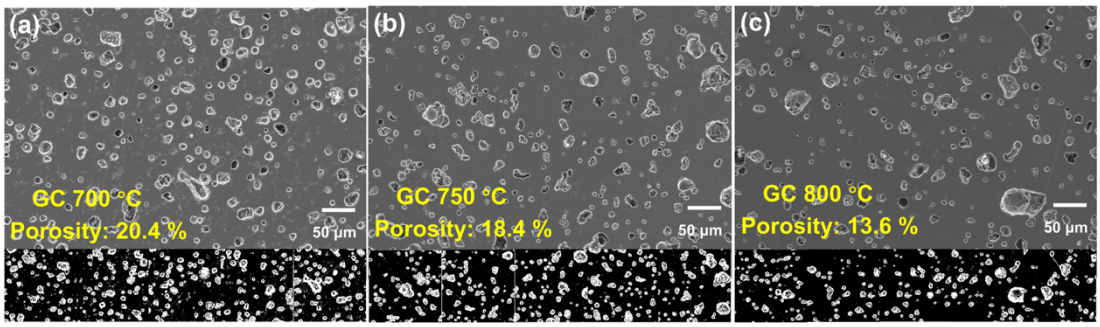

Fig. S31 SEM micrographs and related porosity results of GC sintered at (a) 700 ºC, (b) 750 ºC, and (c) 800 ºC for 2 hours.

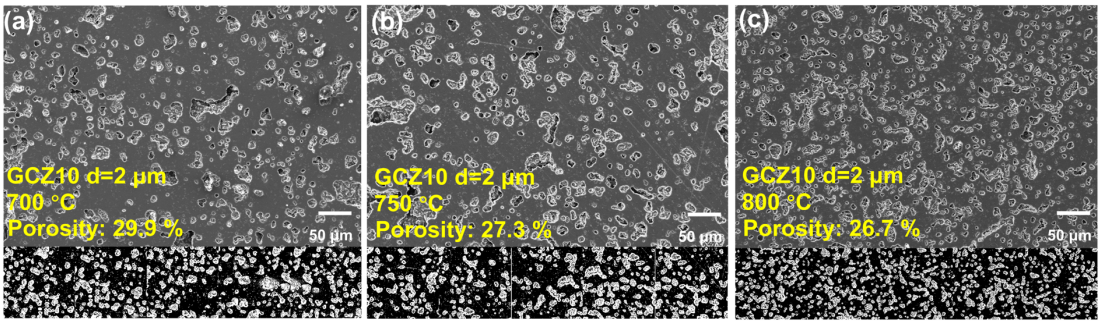

Fig. S32 SEM micrographs and related porosity results of GCZ10, d=2 µm sintered at (a) 700 ºC, (b) 750 ºC, and (c) 800 ºC for 2 hours.

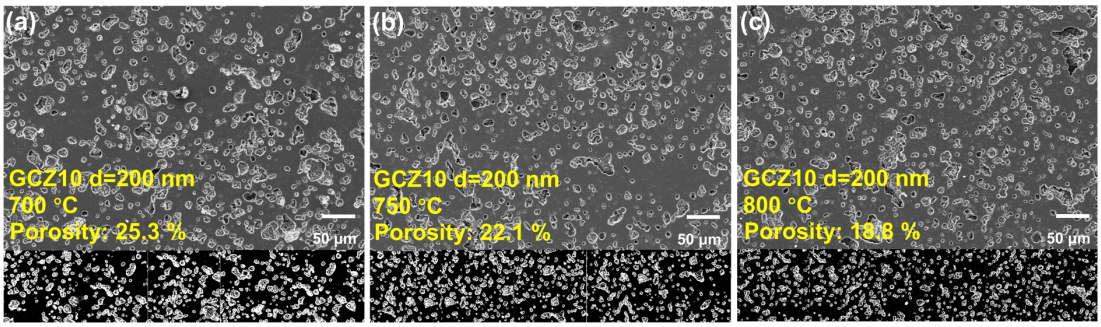

Fig. S33 SEM micrographs and related porosity results of GCZ10, d=200 nm sintered at (a) 700 ºC, (b) 750 ºC, and (c) 800 ºC for 2 hours.

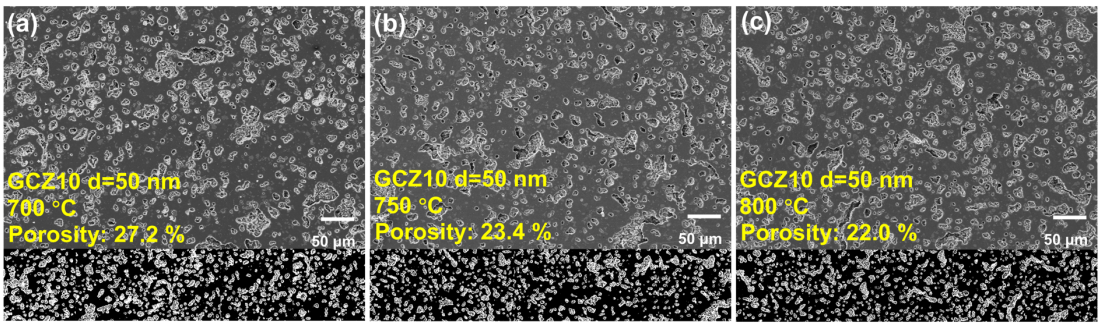

Fig. S34 SEM micrographs and related porosity results of GCZ10, d=50 nm sintered at (a) 700 ºC, (b) 750 ºC, and (c) 800 ºC for 2 hours.

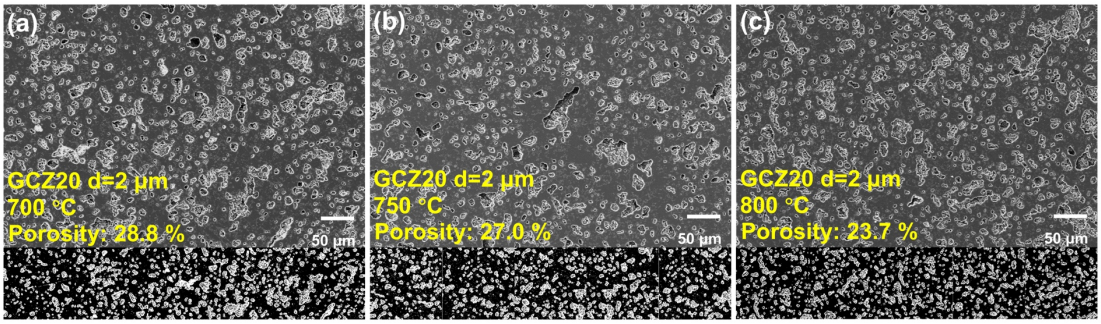

Fig. S35 SEM micrographs and related porosity results of GCZ20, d=2 µm sintered at (a) 700 ºC, (b) 750 ºC, and (c) 800 ºC for 2 hours.

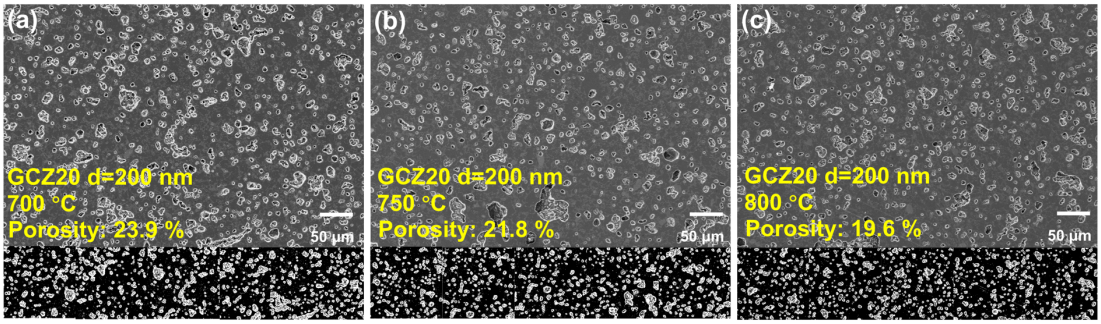

Fig. S36 SEM micrographs and related porosity results of GCZ20, d=200 nm sintered at (a) 700 ºC, (b) 750 ºC, and (c) 800 ºC for 2 hours.

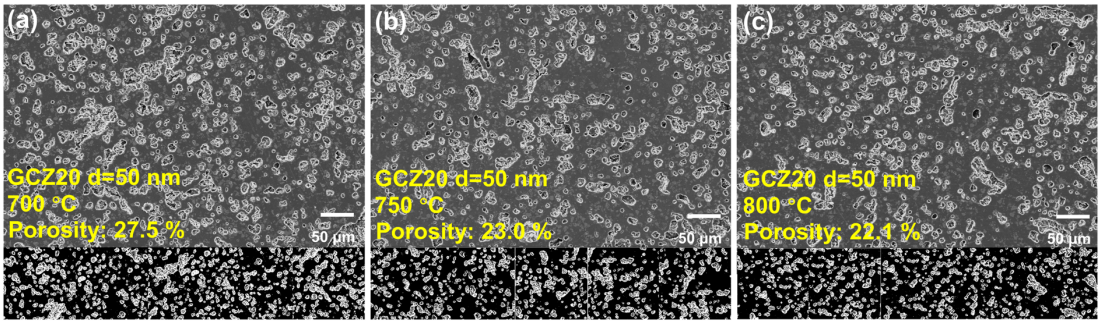

Fig. S37 SEM micrographs and related porosity results of GCZ20, d=50 nm sintered at (a) 700 ºC, (b) 750 ºC, and (c) 800 ºC for 2 hours.

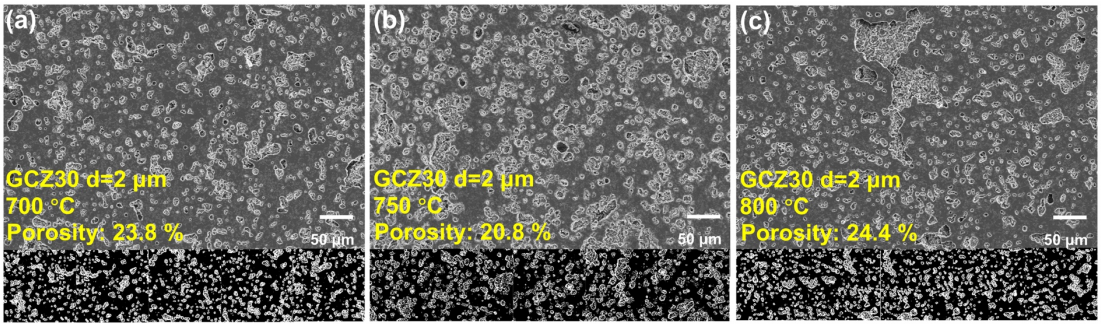

Fig. S38 SEM micrographs and related porosity results of GCZ30, d=2 µm sintered at (a) 700 ºC, (b) 750 ºC, and (c) 800 ºC for 2 hours.

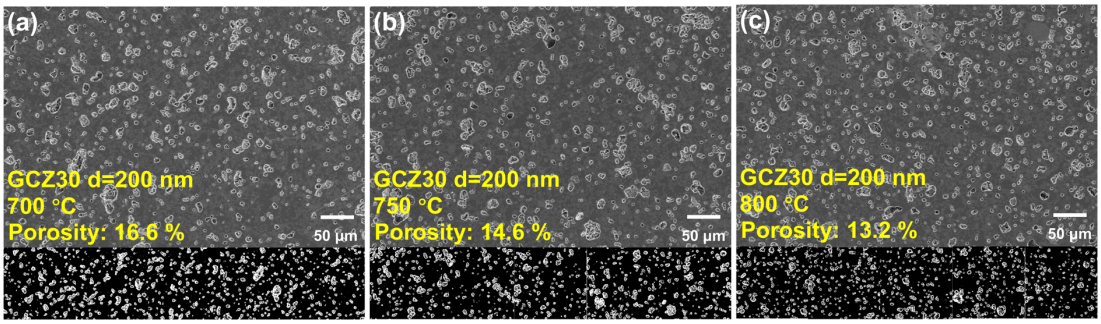

Fig. S39 SEM micrographs and related porosity results of GCZ30, d=200 nm sintered at (a) 700 ºC, (b) 750 ºC, and (c) 800 ºC for 2 hours.

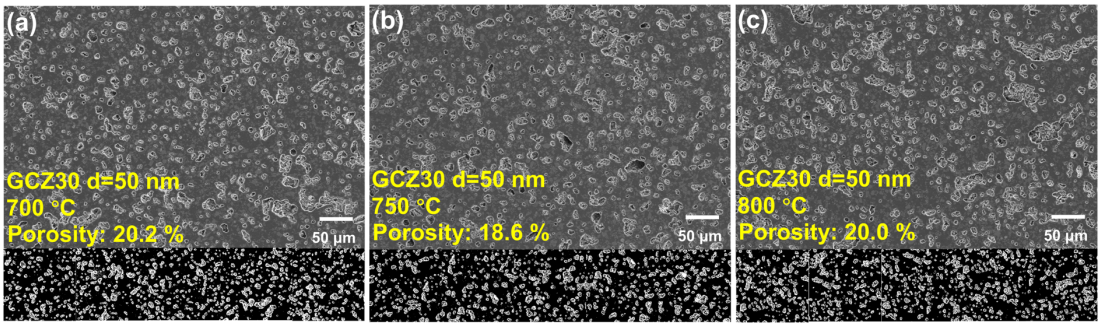

Fig. S40 SEM micrographs and related porosity results of GCZ30, d=50 nm sintered at (a) 700 ºC, (b) 750 ºC, and (c) 800 ºC for 2 hours.

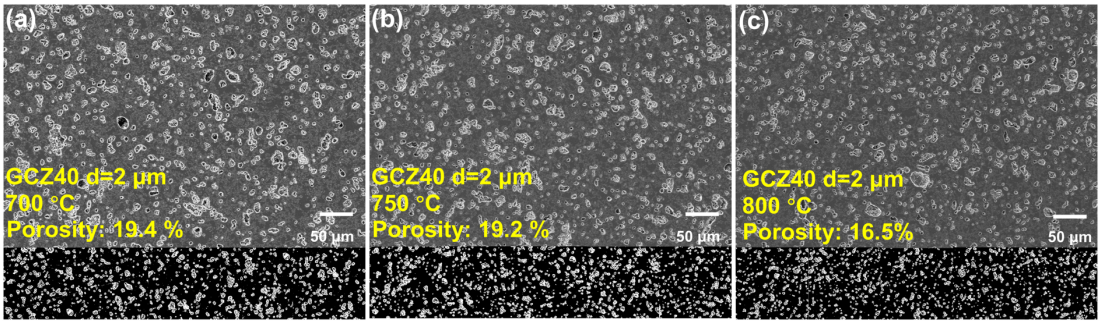

Fig. S41 SEM micrographs and related porosity results of GCZ40, d=2 µm sintered at (a) 700 ºC, (b) 750 ºC, and (c) 800 ºC for 2 hours.

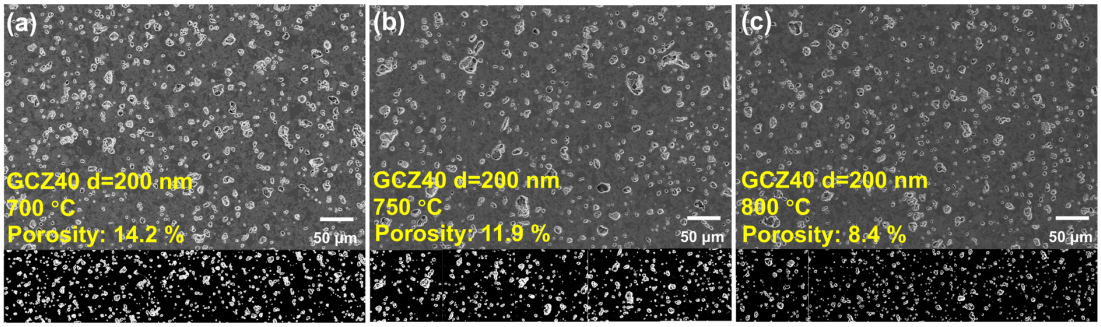

Fig. S42 SEM micrographs and related porosity results of GCZ40, d=200 nm sintered at (a) 700 ºC, (b) 750 ºC, and (c) 800 ºC for 2 hours.

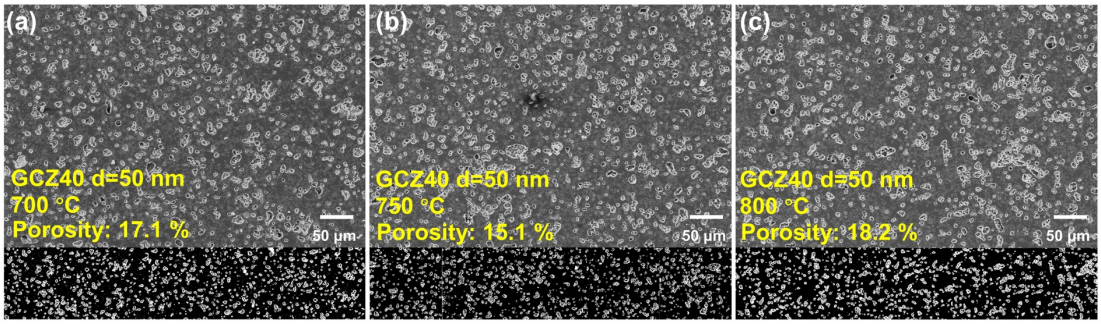

Fig. S43 SEM micrographs and related porosity results of GCZ40, d=50 nm sintered at (a) 700 ºC, (b) 750 ºC, and (c) 800 ºC for 2 hours.

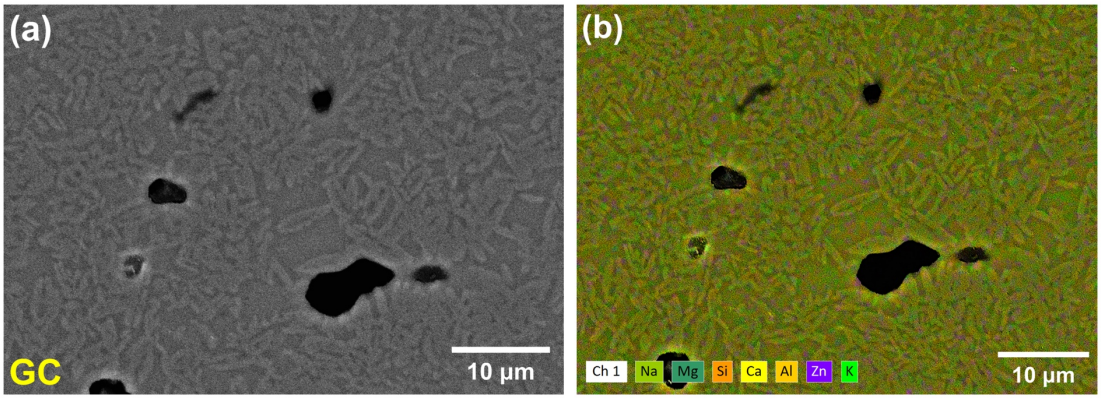

Fig. S44 (a) Backscattered SEM micrograph and (b) elemental distribution (EDS mapping) of GC after heat treatment at 850 ºC for 4 hours.

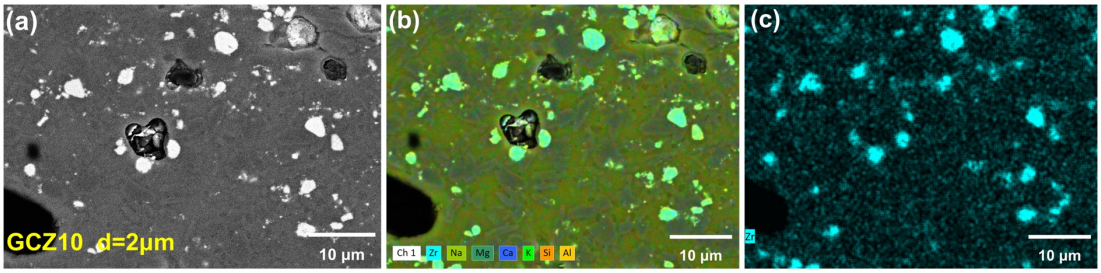

Fig. S45 (a) Backscattered SEM micrograph, (b) elemental distribution (EDS mapping) and (c) distribution of zirconium of GCZ10, d=2 µm after heat treatment at 850 ºC for 4 hours.

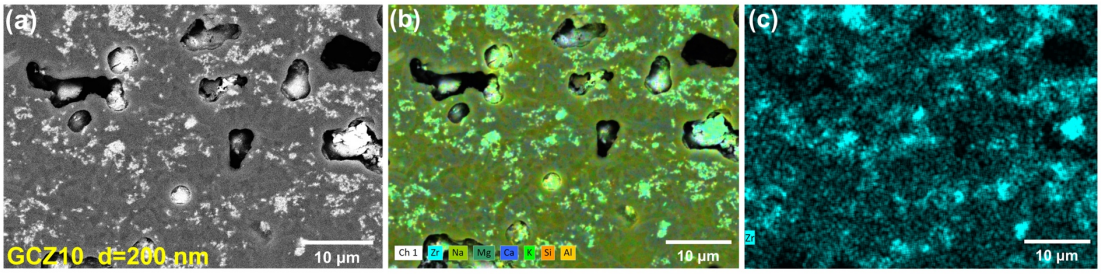

Fig. S46 (a) Backscattered SEM micrograph, (b) elemental distribution (EDS mapping) and (c) distribution of zirconium of GCZ10, d=200 nm after heat treatment at 850 ºC for 4 hours.

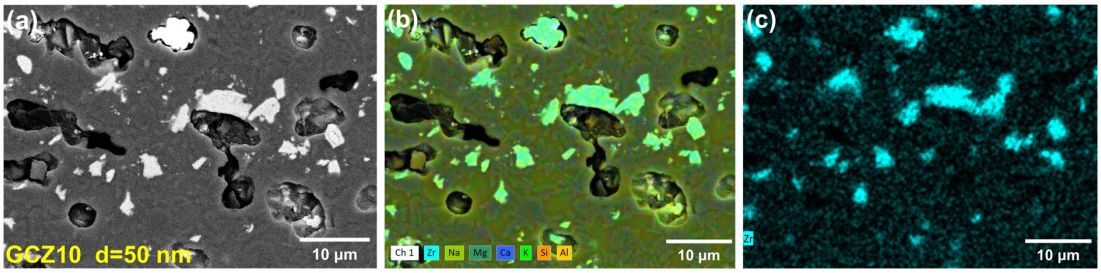

Fig. S47 (a) Backscattered SEM micrograph, (b) elemental distribution (EDS mapping) and (c) distribution of zirconium of GCZ10, d=50 nm after heat treatment at 850 ºC for 4 hours.

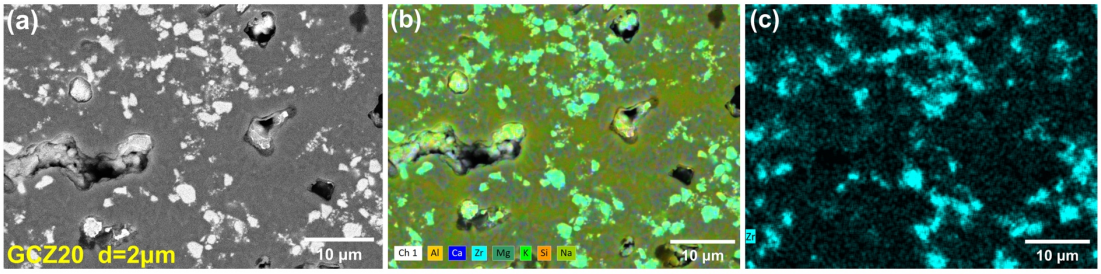

Fig. S48 (a) Backscattered SEM micrograph, (b) elemental distribution (EDS mapping) and (c) distribution of zirconium of GCZ20, d=2µm after heat treatment at 850 ºC for 4 hours.

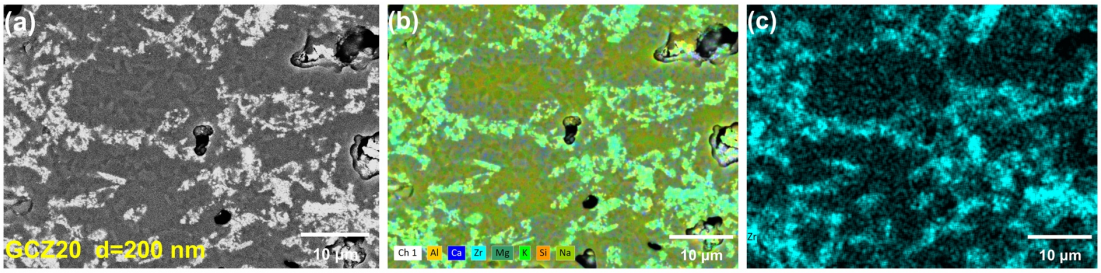

Fig. S49 (a) Backscattered SEM micrograph, (b) elemental distribution (EDS mapping) and (c) distribution of zirconium of GCZ20, d=200 nm after heat treatment at 850 ºC for 4 hours.

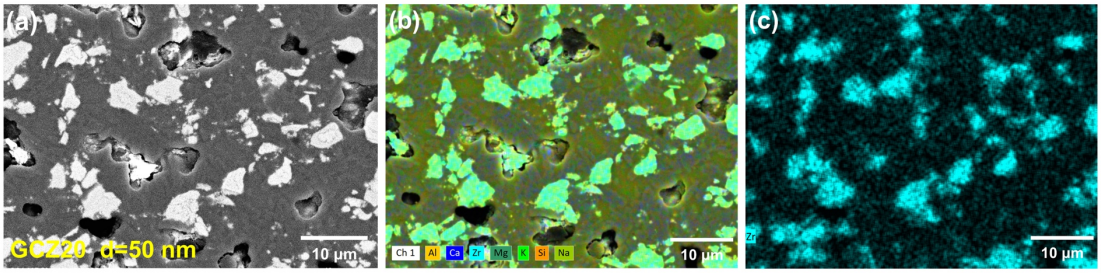

Fig. S50 (a) Backscattered SEM micrograph, (b) elemental distribution (EDS mapping) and (c) distribution of zirconium of GCZ20, d=50 nm after heat treatment at 850 ºC for 4 hours.

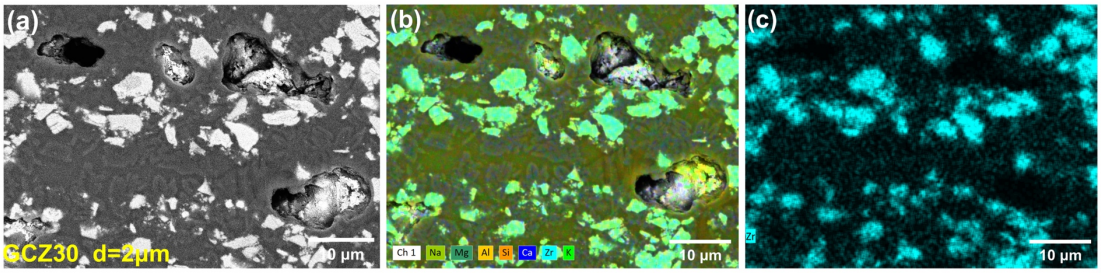

Fig. S51 (a) Backscattered SEM micrograph, (b) elemental distribution (EDS mapping) and (c) distribution of zirconium of GCZ30, d=2 µm after heat treatment at 850 ºC for 4 hours.

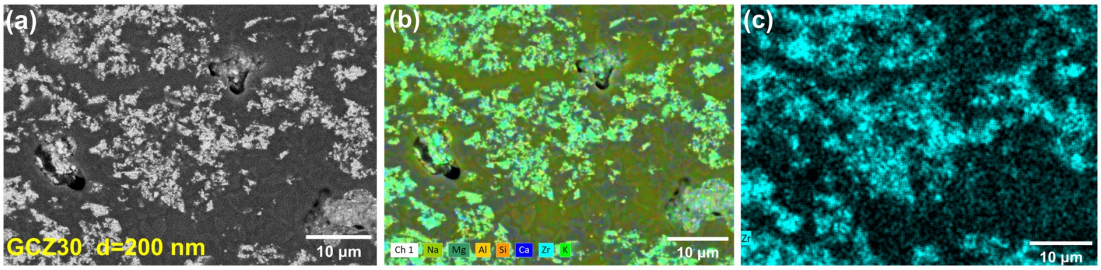

Fig. S52 (a) Backscattered SEM micrograph, (b) elemental distribution (EDS mapping) and (c) distribution of zirconium of GCZ30, d=200 nm after heat treatment at 850 ºC for 4 hours.

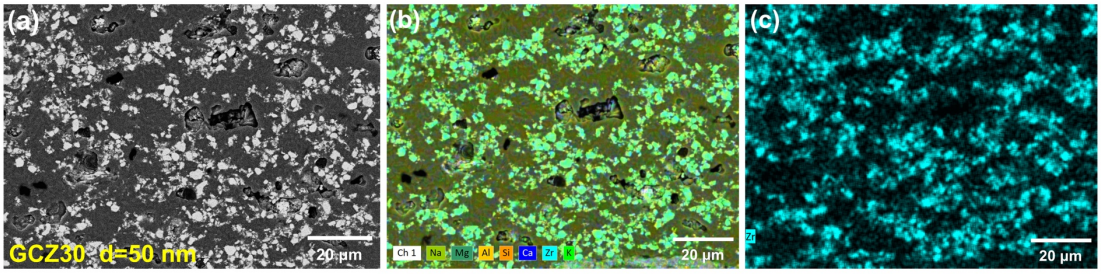

Fig. S53 (a) Backscattered SEM micrograph, (b) elemental distribution (EDS mapping) and (c) distribution of zirconium of GCZ30, d=50 nm after heat treatment at 850 ºC for 4 hours.

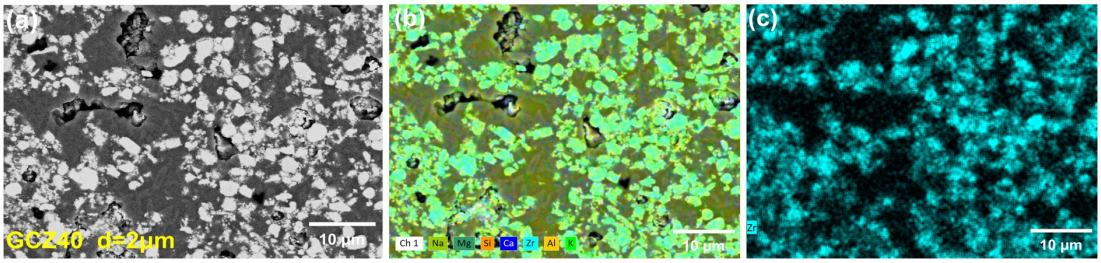

Fig. S54 (a) Backscattered SEM micrograph, (b) elemental distribution (EDS mapping) and (c) distribution of zirconium of GCZ40, d=2 µm after heat treatment at 850 ºC for 4 hours.

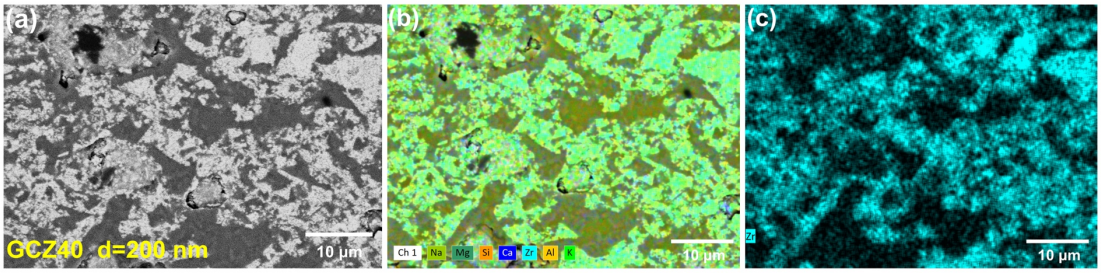

Fig. S55. (a) Backscattered SEM micrograph, (b) elemental distribution (EDS mapping) and (c) distribution of zirconium of GCZ40, d=200 nm after heat treatment at 850 ºC for 4 hours.

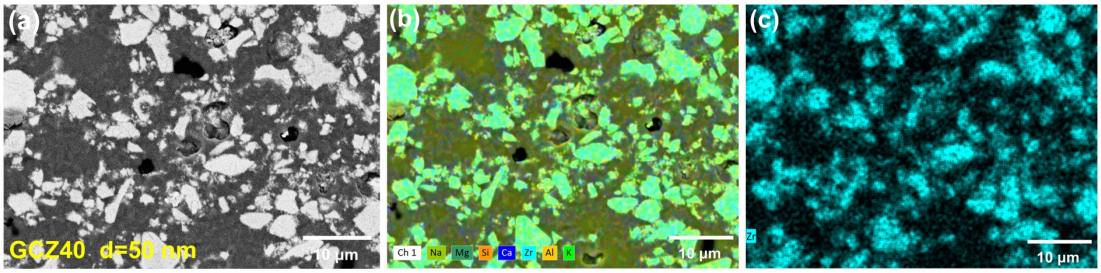

Fig. S56 (a) Backscattered SEM micrograph, (b) elemental distribution (EDS mapping) and (c) distribution of zirconium of GCZ40, d=50 nm after heat treatment at 850 ºC for 4 hours.

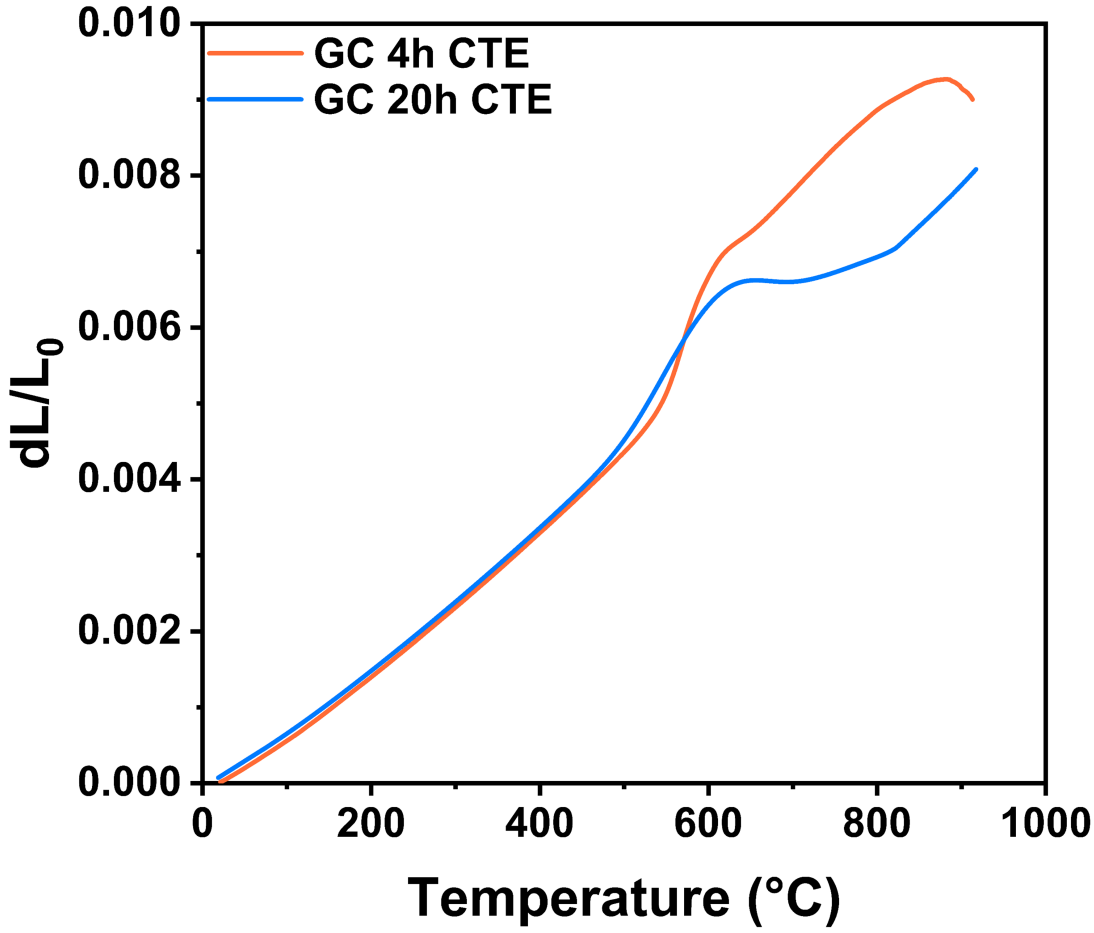

Fig. S57 Dilatometric thermograph of 4h and 20h heat-treated GC samples.

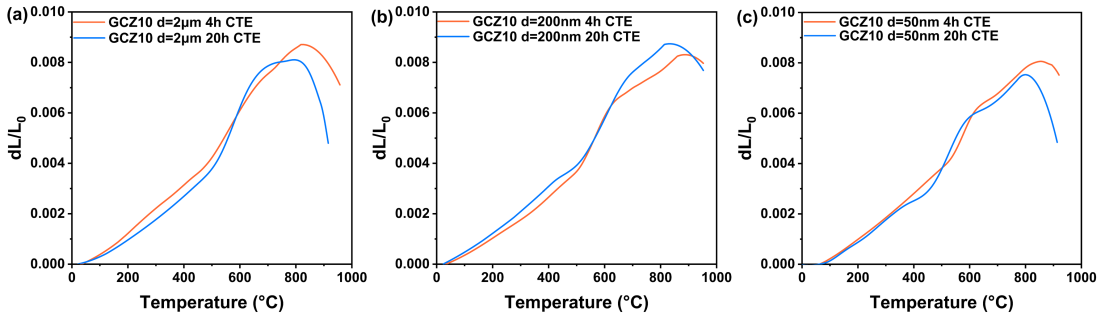

Fig. S58 Dilatometric thermograph of 4h and 20h heat-treated (a) GCZ10, d=2 µm, (b) GCZ10, d=200 nm and (c) GCZ10, d=50 nm samples.

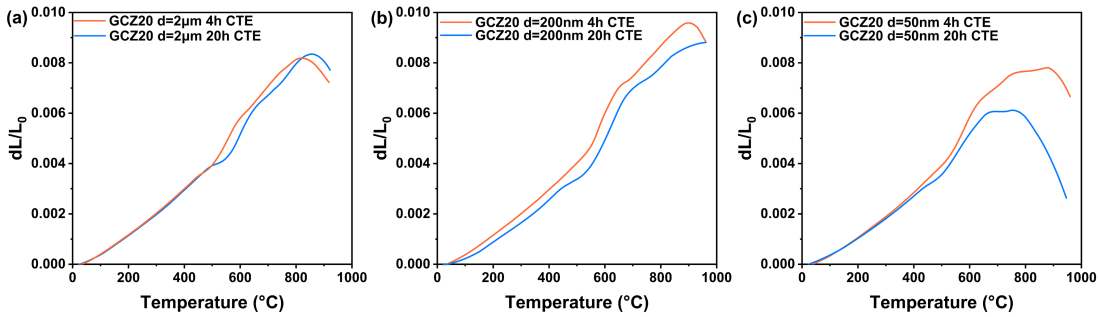

Fig. S59 Dilatometric thermograph of 4h and 20h heat-treated (a) GCZ20, d=2 µm, (b) GCZ20, d=200 nm and (c) GCZ20, d=50 nm samples.

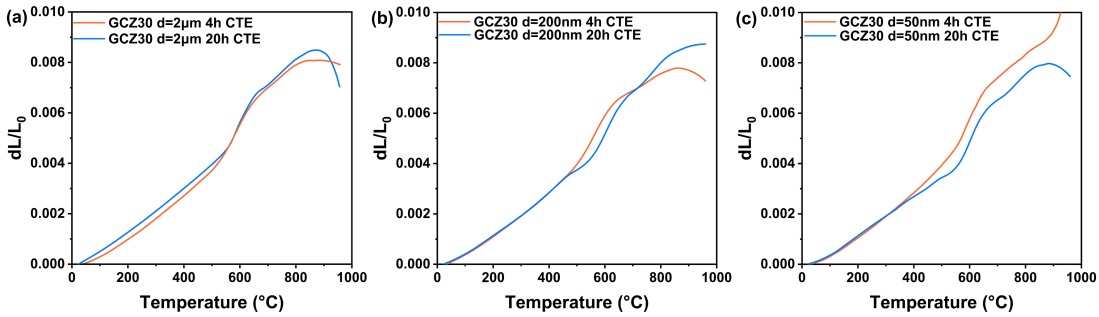

Fig. S60 Dilatometric thermograph of 4h and 20h heat-treated (a) GCZ30, d=2 μm, (b) GCZ30, d=200 nm and (c) GCZ30, d=50 nm samples.

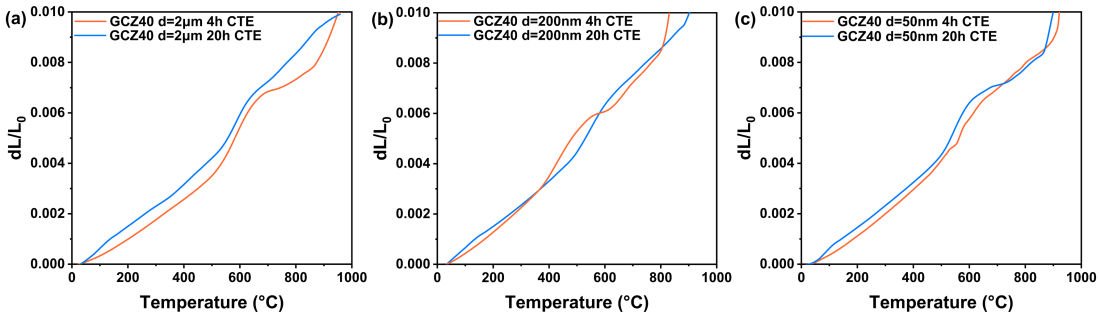

Fig. S61 Dilatometric thermograph of 4h and 20h heat-treated (a) GCZ40, d=2 µm, (b) GCZ40, d=200 nm and (c) GCZ40, d=50 nm samples.

Table S1 The content of each component of GC glass (elements concentration %)

Components	SiO_2	CaO	ZnO	MgO	Na_2O	Al_2O_3	SrO	K_2O	TiO_2	ZrO_2
GC	52.4	15.1	9.5	7.6	5.6	3.4	2.6	1.9	1.2	0.6